Numerical studies of real-gas effects on two-dimensional hypersonic shock-wave/boundary-layer interaction

Gregory H. Furumoto,[a] Xiaolin Zhong, and John C. Skiba
Department of Mechanical and Aerospace Engineering, University of California, Los Angeles, California 90095

(Received 1 March 1996; accepted 29 September 1996)

Nonequilibrium real-gas effects on surface heating rates, skin friction, and flow field unsteadiness of two-dimensional hypersonic shock-wave/boundary-layer interaction were studied by numerical simulations. The unsteady Navier–Stokes equations with nonequilibrium vibrational and chemical models for five-species air were solved by a finite-volume second-order TVD scheme together with a third-order semi-implicit Runge–Kutta scheme. Two cases of high-enthalpy shock/boundary layer interaction problems were studied in this paper. The freestream enthalpy was high enough to produce vibrational excitation and dissociation/recombination chemistry behind the shock. The first case was a steady two-dimensional shock/boundary layer interaction on a flat plate with a mixture of N_2 and O_2 in the freestream. It was found that the real gas effects reduce the size of the shock induced separation bubble and the magnitude of the surface heating rates. The second case was a self-sustained unsteady type IV shock–shock interference heating of a pure N_2 flow over a cylinder. The results showed that type IV shock–shock interference heating flows with real-gas effects are inherently unsteady. Vortices are generated and shed off near the jet impingement point. This periodic shedding of the vortices contributes to the self-sustained oscillations of both the jet and other parts of the flow fields. In addition, the real-gas effects reduce the level of peak surface heating and peak surface pressure due to endothermic real-gas effects. © *1997 American Institute of Physics.* [S1070-6631(97)02301-5]

I. INTRODUCTION

Shock-wave/boundary layer interactions and shock–shock interference heating problems occur in many external and internal flow fields around hypersonic vehicles, such as the one shown in Fig. 1. Understanding such shock interactions is vital for the design of hypersonic vehicles because they often introduce severe local heating and induce boundary separations. Two types of shock interactions, shock/boundary layer interactions and type IV shock interference heating, were studied in this paper.

The first type of shock interactions is the shock/boundary layer interaction on a flat plate, where an incident oblique shock is reflected by the surface of the plate. Figure 2 shows a schematic of a steady shock-wave reflection interaction with the viscous boundary layer. The large adverse pressure gradient due to the incident shock hitting the wall causes the boundary layer to separate. When the boundary layer reattaches, a reattachment compression shock is formed. Local heating rates to the surface increase considerably at the region of the shock impingement.

The second type of shock interactions is the shock–shock interference heating problems created by an impinging oblique shock intersecting the freestream bow shock ahead of a body. These interference heating problems were classified by Edney[1] into six types according to the shock-impinging location relative to the stagnation point on the surface. Among them, the type IV interaction, which corresponds to the case of impinging point near the stagnation point, has received the most attention because it creates the most complex flow pattern and most severe heating to the surface. Figure 3 shows a schematic of the type IV interaction. This interaction creates a transmitted shock which impinges upon the lower bow shock behind the initial impinging oblique shock. Behind this transmitted shock, which is weaker than either bow shock, a supersonic jet is formed in the surrounding subsonic flow. This jet impinges on the body, ending in a terminating strong shock. At the jet impingement point, extremely high surface pressures and heating rates are encountered.[2–5] As the jet flow is expanded over the surface, it once again becomes supersonic. This creates a shear layer along the body between the flow from the jet and the subsonic bulk flow behind the bow shock. This type of interaction has been shown to be inherently unstable[4,6,7] in ideal gas flows.

To date, most studies of the shock interactions have been limited to ideal gas flows for both shock/boundary layer interaction,[8,9] and shock–shock interference heating problems. The ideal gas type IV interference heating problem has been extensively studied experimentally and analytically,[3,10] and numerically.[4–7] For high-enthalpy hypersonic shock/boundary layer interaction, however, real-gas effects become significant and they need to be considered for many of these flow studies. Real-gas effects can have a noticeable impact on flow features, such as the shock stand off distance in a blunt body flow,[11] which is reduced due to real-gas effects, and parameters such as surface heating rates, which can be either reduced or enhanced depending on the nature of the chemical nonequilibrium.

Because of their importance, real-gas effects have recently been the focus of several studies. For two-dimensional steady shock/boundary layer interactions, Ballaro and

[a]Electronic mail: furumoto@seas.ucla.edu

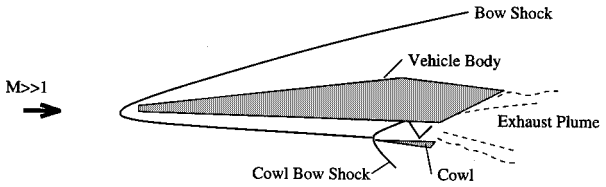

FIG. 1. Typical hypersonic vehicle and associated shock interaction.

Anderson,[12] and Grumet *et al.*[13] performed numerical studies of flow at a scramjet inlet with real-gas effects. A partially dissociated freestream was assumed to simulate conditions at an inlet behind the bow shock of a vehicle. They found that the recombination of species at the wall enhanced the surface heat flux. Type IV shock–shock interactions were studied numerically by Prabhu *et al.*[14] using an equilibrium chemistry model. More recently, Sanderson[15] experimentally and analytically examined the nonequilibrium real-gas effects on type IV interference heating flows. A numerical study was done by Brück[16] on steady type IV shock–shock interference heating flow with nonequilibrium real-gas effects. The effects of nonequilibrium and impinging shock location on steady flow structure and surface pressure and heat flux were investigated. These real-gas studies, however, have only addressed the issue of steady flows. Though ideal gas shock interference has been found to be unsteady and the unsteadiness has strong effects on surface heating rates, so far, no numerical work in studying real-gas effects in unsteady shock interactions has been done, to the authors' knowledge.

In this paper, the steady and self-sustained unsteady shock/boundary layer interaction with real-gas effects was studied by time-accurate computations of the Navier–Stokes equations with nonequilibrium real-gas models. The test cases were two-dimensional steady shock/boundary layer interaction on a flat plate and inherently unsteady type IV shock–shock interference heating problems. The high freestream enthalpy for these two cases was sufficiently high to produce vibrational excitation and dissociation/recombination chemistry behind the shock. The effects of the thermo-chemical nonequilibrium on the flow characteristics were investigated by using currently available thermal and chemical nonequilibrium models. The viscous nonequilibrium flows were modeled by the multi-component Navier–Stokes equations with a multi-temperature model for nonequilibrium vibrational and chemical modes, following the models of Candler,[17] Gökçen,[18] and Park.[19] The chemical model used in this paper was appropriate for air temperatures below 8000−9000 K because ionization of the gas was neglected.

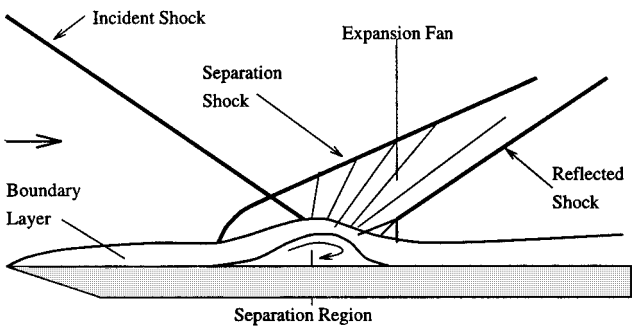

FIG. 2. Schematic for steady shock-wave/boundary layer interaction.

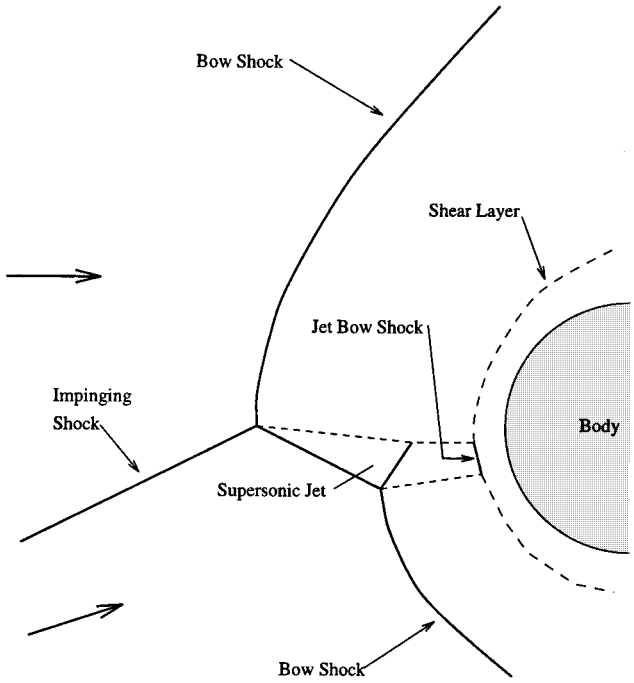

FIG. 3. Schematic of a shock–shock interference heating flow field.

Time-accurate numerical solutions were used to study such complex flow problems. The numerical accuracy of the solutions are estimated by grid refinement studies. The governing conservation equations for the unsteady real-gas flows were computed by a second-order TVD scheme with the Roe approximate Riemann solver. The stiffness of the source terms were removed by using an Additive Semi-implicit Runge–Kutta method of Zhong[20] for temporal discretization of the equations.

II. PHYSICAL MODEL

A. Equations of motion

The multicomponent Navier–Stokes Equations in conservative form along with the vibrational energy equations are

$$\frac{\partial \rho_i}{\partial t}+\frac{\partial}{\partial x}(\rho_i u+j_{ix})+\frac{\partial}{\partial y}(\rho_i v+j_{iy})=w_i, \tag{1}$$

$$\frac{\partial(\rho u)}{\partial t}+\frac{\partial}{\partial x}(\rho u^2+p-\tau_{xx})+\frac{\partial}{\partial y}(\rho uv-\tau_{xy})=0, \tag{2}$$

$$\frac{\partial(\rho v)}{\partial t}+\frac{\partial}{\partial x}(\rho uv-\tau_{xy})+\frac{\partial}{\partial y}(\rho v^2+p-\tau_{yy})=0, \tag{3}$$

$$\frac{\partial E_v}{\partial t}+\frac{\partial}{\partial x}(uE_v+q_{vx})+\frac{\partial}{\partial y}(vE_v+q_{vy})=w_v, \tag{4}$$

TABLE I. Thermal properties and viscosity model for a five species air model.

Species	Thermal properties θ_v (K)	$h°$ (J/kg)	Coefficients for viscosity model A_i	B_i	C_i
N_2	3390	0	0.5673×10^{-6}	0.7310	-0.1510×10^{2}
O_2	2270	0	0.2000×10^{-5}	0.6980	-0.1476×10^{2}
NO	2740	2.996×10^{6}	0.1491×10^{-6}	0.7180	-0.1496×10^{2}
N	⋯	3.3662×10^{7}	0.3171×10^{-1}	0.3475	-0.1391×10^{2}
O	⋯	1.543×10^{7}	0.1374×10^{-1}	0.5139	-0.1374×10^{2}

$$\frac{\partial E}{\partial t}+\frac{\partial}{\partial x}[u(E+p)-u\tau_{xx}-v\tau_{xy}+q_x]+\frac{\partial}{\partial y}[v(E+p)-u\tau_{xy}-v\tau_{yy}+q_y]=0, \tag{5}$$

where E_v and E are the vibrational and total energies per unit volume, respectively. The w_i's are the chemical source terms for species i, and w_v is the source term for the vibrational mode.

B. Equations of state

The system is taken to be a mixture of thermally perfect gases with the following equation of state:

$$p=\rho R T_t, \tag{6}$$

where p and ρ are the bulk pressure and density, respectively, T_t is the translational temperature, and R is the mass averaged gas constant defined as

$$R=\sum_i \frac{\rho_i}{\rho}R_i; \tag{7}$$

R_i is the species specific gas constant.

The nonequilibrium vibrational energy mode is modeled by a separate temperature, T_v.[17,18,21] The internal energy equation for a diatomic species is

$$e_i=\frac{5}{2}R_iT_t+e_{vi}+h_i^\circ, \tag{8}$$

$$e_{vi}=R_i\frac{\theta_{vi}}{e^{\theta_{vi}/T_v}-1}, \tag{9}$$

where θ_{vi} is the characteristic vibrational temperature of species i. These values are given in Table I. For monatomic species:

$$e_i=\frac{3}{2}R_iT_t+h_i^\circ. \tag{10}$$

In the above, h_i° are the species heats of formation, which are given in Table I.

The equations for total energy per unit volume are

$$E_v=\sum_i \rho_i e_{vi}, \tag{11}$$

$$E=\sum_i \rho_i e_i+\rho\frac{u^2+v^2}{2}. \tag{12}$$

C. Constitutive relations

The viscous stresses are modeled by the Navier–Stokes equations:

$$\tau_{xx}=\frac{2}{3}\mu\left[2\frac{\partial u}{\partial x}-\frac{\partial v}{\partial y}\right], \tag{13}$$

$$\tau_{xy}=\mu\left[\frac{\partial u}{\partial y}+\frac{\partial v}{\partial x}\right], \tag{14}$$

$$\tau_{yy}=\frac{2}{3}\mu\left[2\frac{\partial v}{\partial y}-\frac{\partial u}{\partial x}\right]. \tag{15}$$

For chemically reacting flow, multicomponent diffusion is approximately modeled by Fick's Law for binary diffusion:

$$j_{ix}=-\rho D\frac{\partial(\rho_i/\rho)}{\partial x}, \tag{16}$$

$$j_{iy}=-\rho D\frac{\partial(\rho_i/\rho)}{\partial y}, \tag{17}$$

Diffusion due to thermal and pressure gradients is neglected for simplicity.

Heat conductivity is modeled by Fourier's Law:

$$q_x=-\kappa_t\frac{\partial T_t}{\partial x}-\kappa_v\frac{\partial T_v}{\partial x}+\sum_i j_{ix}h_i, \tag{18}$$

$$q_y=-\kappa_t\frac{\partial T_t}{\partial y}-\kappa_v\frac{\partial T_v}{\partial y}+\sum_i j_{iy}h_i, \tag{19}$$

with the total enthalpy, h_i, being given by

$$h_i=e_i+R_iT_t. \tag{20}$$

The transport coefficients need to be modeled for a gas mixture and, where appropriate, for the nonequilibrium energy modes. Individual species viscosities (μ_i) are calculated using a curve fit model presented by Moss:[22]

$$\mu_i=\exp[(A_i\ln T_t+B_i)\ln T_t+C_i], \tag{21}$$

where A_i, B_i, and C_i are tabulated empirical constants given in Table I. The viscosity of the gas mixture is then computed according to Wilke's formulation:[23]

$$\mu=\sum_i \frac{X_i\mu_i}{\Sigma_j X_j\phi_{ij}}, \tag{22}$$

$$\phi_{ij}=\frac{\left[1+\left(\frac{\mu_i}{\mu_j}\right)^{1/2}\left(\frac{\mathscr{M}_j}{\mathscr{M}_i}\right)^{1/4}\right]^2}{\left[8\left(1+\frac{\mathscr{M}_i}{\mathscr{M}_j}\right)\right]^{1/2}}, \tag{23}$$

where $\mathscr{M}_i$ is the molecular weight and X_i is the mole fraction of species i, respectively.

The binary diffusion coefficient, D, is computed by assuming a constant Schmidt number:[18]

$$Sc=\frac{\mu}{\rho D}=0.5. \tag{24}$$

While more accurate, multicomponent models are available in the literature, for example in Ref. 24, this simple model was used due to its higher computational efficiency. Additionally, the shock–shock interaction cases presented below are two component flows. Because the degree of N_2 dissociation in those cases was not extremely high, around 10%, the effects of mass diffusion were not expected to be very large.

The individual species translational heat conduction coefficients (κ_{ti}) are given by Eucken's relation:[21]

$$\kappa_{ti}=\frac{5}{2}\mu_i c_{vti}, \tag{25}$$

where

$$c_{vti}=\frac{5}{2}R_i \quad \text{for diatomic}$$

and

$$c_{vti}=\frac{3}{2}R_i \quad \text{for monatomic.} \tag{26}$$

The overall heat conductivity coefficient is then calculated using Wilke's formula in a similar fashion to the one for the viscosity coefficient.[9]

The thermal conductivity associated with the vibrational mode is given by[18]

$$\kappa_v=\sum\left(\frac{\rho_i}{\rho}\right)\mu_i c_{vvi}, \tag{27}$$

where the sum is taken over the diatomic species only, and

$$c_{vvi}=\frac{R_i(\theta_{vi}/T_v)^2 e^{\theta_{vi}/T_v}}{(e^{\theta_{vi}/T_v}-1)^2}. \tag{28}$$

D. Source terms

Finite-rate chemistry of air is modeled using a five species model (N_2, O_2, NO, N, O) without ionization. For the test cases considered in this paper, the temperatures are not expected to exceed 9000 K, which is the threshold for ionization.[9] The five species reaction model is given as

$$N_2+M_i \rightleftharpoons N+N+M_i, \tag{29}$$

$$O_2+M_i \rightleftharpoons O+O+M_i, \tag{30}$$

$$NO+M_i \rightleftharpoons N+O+M_i, \tag{31}$$

$$N_2+O \rightleftharpoons NO+N, \tag{32}$$

$$NO+O \rightleftharpoons O_2+N, \tag{33}$$

where M_i denotes any of the i species. Reaction rates for each of these 17 reactions can be written as

$$\mathscr{R}_1=\sum_i k_{b1i}[N]^2[M_i]-k_{f1i}[N_2][M_i], \tag{34}$$

$$\mathscr{R}_2=\sum_i k_{b2i}[O]^2[M_i]-k_{f2i}[O_2][M_i], \tag{35}$$

$$\mathscr{R}_3=\sum_i k_{b3i}[N][O][M_i]-k_{f3i}[NO][M_i], \tag{36}$$

$$\mathscr{R}_4=k_{b4}[NO][N]-k_{f4}[N_2][O], \tag{37}$$

$$\mathscr{R}_5=k_{b5}[O_2][N]-k_{f5}[NO][O]. \tag{38}$$

TABLE II. Dissociation/recombination rate coefficients for a Dunn–Kang 5 species air model.

Reaction	M_i	k	Reaction rate coefficients: $k=CT_x^{\eta}\exp(-\theta_d/T_x)$ $C(\mathrm{m^3-kmol-s})$	η	θ_d (K)	T_x
$N_2+M_i\rightarrow N+N+M_i$	N_2	k_{f11}	4.80×10^{14}	−0.5	113000	$\sqrt{T_vT_t}$
	O_2	k_{f12}	1.92×10^{14}	−0.5	113000	$\sqrt{T_vT_t}$
	NO	k_{f13}	1.92×10^{14}	−0.5	113000	$\sqrt{T_vT_t}$
	N	k_{f14}	4.16×10^{19}	−1.5	113000	$\sqrt{T_vT_t}$
	O	k_{f15}	1.92×10^{14}	−0.5	113000	$\sqrt{T_vT_t}$
$N+N+M_i\rightarrow N_2+M_i$	N_2	k_{b11}	2.72×10^{10}	−0.5	0	T_t
	O_2	k_{b12}	1.10×10^{10}	−0.5	0	T_t
	NO	k_{b13}	1.10×10^{10}	−0.5	0	T_t
	N	k_{b14}	2.27×10^{15}	−1.5	0	T_t
	O	k_{b15}	1.10×10^{10}	−0.5	0	T_t
$O_2+M_i\rightarrow O+O+M_i$	N_2	k_{f21}	7.21×10^{15}	−1.0	59500	$\sqrt{T_vT_t}$
	O_2	k_{f22}	3.25×10^{16}	−1.0	59500	$\sqrt{T_vT_t}$
	NO	k_{f23}	3.61×10^{15}	−1.0	59500	$\sqrt{T_vT_t}$
	N	k_{f24}	3.61×10^{15}	−1.0	59500	$\sqrt{T_vT_t}$
	O	k_{f25}	9.02×10^{16}	−1.0	59500	$\sqrt{T_vT_t}$
$O+O+M_i\rightarrow O_2+M_i$	N_2	k_{b21}	6.00×10^{9}	−0.5	0	T_t
	O_2	k_{b22}	2.70×10^{10}	−0.5	0	T_t
	NO	k_{b23}	3.00×10^{9}	−0.5	0	T_t
	N	k_{b24}	3.00×10^{9}	−0.5	0	T_t
	O	k_{b25}	7.50×10^{10}	−0.5	0	T_t
$NO+M_i\rightarrow N+O+M_i$	N_2	k_{f31}	3.97×10^{17}	−1.5	75500	$\sqrt{T_vT_t}$
	O_2	k_{f32}	3.97×10^{17}	−1.5	75500	$\sqrt{T_vT_t}$
	NO	k_{f33}	7.94×10^{18}	−1.5	75500	$\sqrt{T_vT_t}$
	N	k_{f34}	7.94×10^{18}	−1.5	75500	$\sqrt{T_vT_t}$
	O	k_{f35}	7.94×10^{18}	−1.5	75500	$\sqrt{T_vT_t}$
$N+O+M_i\rightarrow NO+M_i$	N_2	k_{b31}	1.00×10^{14}	−1.5	0	T_t
	O_2	k_{b32}	1.00×10^{14}	−1.5	0	T_t
	NO	k_{b33}	2.00×10^{15}	−1.5	0	T_t
	N	k_{b34}	2.00×10^{15}	−1.5	0	T_t
	O	k_{b35}	2.00×10^{15}	−1.5	0	T_t
$N_2+O\rightarrow NO+N$	⋯	k_{f4}	6.74×10^{10}	0	38000	$\sqrt{T_vT_t}$
$NO+N\rightarrow N_2+O$	⋯	k_{b4}	1.56×10^{10}	0	0	⋯
$NO+O\rightarrow O_2+N$	⋯	k_{f5}	3.18×10^{6}	−1.0	19700	$\sqrt{T_vT_t}$
$O_2+N\rightarrow NO+O$	⋯	k_{b5}	1.30×10^{7}	−1.0	3580	$\sqrt{T_vT_t}$

The rate coefficients (the k_f and k_b's) used in this paper are the Dunn–Kang rate coefficients based on a two temperature model as presented by Häuser *et al.*[25] Both forward and backward rate coefficients are calculated using a modified Arrhenius expression. The translational temperature is used for the backward (recombination) coefficients and a geometrically averaged temperature ($\sqrt{T_tT_v}$) is used for the forward (dissociation) coefficients. The coefficients are given in Table II. With these rate coefficients, expressions for the species source terms can be written as

$$w_1=\mathscr{M}_1(\mathscr{R}_1+\mathscr{R}_4), \tag{39}$$

$$w_2=\mathscr{M}_2(\mathscr{R}_2-\mathscr{R}_5), \tag{40}$$

$$w_3=\mathscr{M}_3(\mathscr{R}_3-\mathscr{R}_4+\mathscr{R}_5), \tag{41}$$

$$w_4=\mathscr{M}_4(-2\mathscr{R}_1-\mathscr{R}_3-\mathscr{R}_4-\mathscr{R}_5), \tag{42}$$

$$w_5=\mathscr{M}_5(-2\mathscr{R}_2-\mathscr{R}_3+\mathscr{R}_4+\mathscr{R}_5). \tag{43}$$

The energy transfer modes considered are translation–vibration coupling, and vibration–dissociation coupling. Other modes were assumed to be negligible in their effect.[18] The vibration–translation modes was modeled using the

Landau–Teller model, which requires an expression for the respective relaxation time associated with the transfer mode.

The expression for vibration–translation coupling is

$$Q_{T-V}=\sum_j \frac{\rho_j R_j \theta_{vj}\left(\frac{1}{e^{\theta_{vj}/T_t}-1}-\frac{1}{e^{\theta_{vj}/T_v}-1}\right)}{\tau_{vj}}, \tag{44}$$

where the sum is taken over the diatomic species only. For the vibrational relaxation time of species j, τ_{vj}, the corrected Millikan and White formula as proposed by Park[19,26] was used. This gives the vibrational time as

$$\tau_{vj}=\langle \tau_{vj}\rangle+\tau_{cj}, \tag{45}$$

with

$$\langle \tau_{vj}\rangle=\frac{\Sigma_i X_i}{\Sigma_i X_i/\tau_{vij}^{MW}} \tag{46}$$

(where the sums are taken over all species),

$$\tau_{vij}^{MW}=\frac{1}{p}\exp[A\mu_{ij}^{-1/2}\theta_{vj}^{4/3}(T_t^{-1/3}-B\mu_{ij}^{1/4})-C], \tag{47}$$

$$A=1.16\times 10^{-3}, \quad B=0.015, \quad C=18.42,$$

and

$$\tau_{cj}=\frac{1}{\overline{c_j}\sigma_v N}, \tag{48}$$

where X_i is the mole fraction of species i, p is in units of atmospheres, θ_{vj} is the characteristic vibrational temperature of species j, μ_{ij} is the reduced mass given by

$$\mu_{ij}=\frac{\mathscr{M}_i\mathscr{M}_j}{\mathscr{M}_j+\mathscr{M}_i}, \tag{49}$$

$\overline{c_j}$ is the mean molecular speed given by

$$\overline{c_j}=\sqrt{\frac{8R_jT_t}{\pi}}, \tag{50}$$

σ_v is the limited collision cross section (in m^2) given by[27,28]

$$\sigma_v=10^{-21}\left(\frac{50\,000}{T_t}\right)^2, \tag{51}$$

and N is the total number density of the gas.

The model used for vibration–dissociation coupling is the one employed by Candler in Ref. 17 and is given by

$$Q_{V-D}=\sum_j w_j\frac{R_j\theta_{vj}}{e^{\theta_{vj}/T_v}-1}, \tag{52}$$

where the sum is taken over the diatomic species only.

The vibrational source term is then

$$w_v=Q_{T-V}+Q_{V-D}. \tag{53}$$

III. NUMERICAL METHOD

The unsteady flow field is solved using a second-order finite-volume TVD scheme for spatial discretization. The source terms is computed via a semi-implicit Runge–Kutta method.[20] The governing equations are written in the conservation law form:

$$\frac{\partial \mathbf{U}}{\partial t}+\frac{\partial}{\partial x}(\mathbf{F}+\mathbf{F_v})+\frac{\partial}{\partial y}(\mathbf{G}+\mathbf{G_v})=\mathbf{W}, \tag{54}$$

where the conserved quantity and source term vectors are

$$\mathbf{U}=\begin{bmatrix}\rho_1\\ \rho_2\\ \rho_3\\ \rho_4\\ \rho_5\\ \rho u\\ \rho v\\ E_v\\ E\end{bmatrix}, \quad \mathbf{W}=\begin{bmatrix}w_1\\ w_2\\ w_3\\ w_4\\ w_5\\ 0\\ 0\\ w_v\\ 0\end{bmatrix}. \tag{55}$$

Inviscid fluxes are

$$\mathbf{F}=\begin{bmatrix}\rho_1 u\\ \rho_2 u\\ \rho_3 u\\ \rho_4 u\\ \rho_5 u\\ \rho u^2+p\\ \rho v u\\ uE_v\\ u(E+p)\end{bmatrix}, \quad \mathbf{G}=\begin{bmatrix}\rho_1 v\\ \rho_2 v\\ \rho_3 v\\ \rho_4 v\\ \rho_5 v\\ \rho uv\\ \rho v^2+p\\ vE_v\\ v(E+p)\end{bmatrix}. \tag{56}$$

Viscous and diffusive fluxes are

$$\mathbf{F_v}=\begin{bmatrix}j_{1x}\\ j_{2x}\\ j_{3x}\\ j_{4x}\\ j_{5x}\\ -\tau_{xx}\\ -\tau_{xy}\\ q_{vx}\\ Q_x\end{bmatrix}, \quad \mathbf{G_v}=\begin{bmatrix}j_{1y}\\ j_{2y}\\ j_{3y}\\ j_{4y}\\ j_{5y}\\ -\tau_{xy}\\ -\tau_{yy}\\ q_{vy}\\ Q_y\end{bmatrix}, \tag{57}$$

where $Q_x=-u\tau_{xx}-v\tau_{xy}+q_x$ and $Q_y=-u\tau_{xy}-v\tau_{yy}+q_y$.

The conservation laws are cast into an integral form in terms of grid-cell averages so that the finite volume technique could be applied:

$$\frac{\partial \mathbf{U}_{ij}}{\partial t}+\frac{1}{V_{ij}}\oint_S \mathbf{E}\cdot d\mathbf{s}=\mathbf{W}_{ij}, \tag{58}$$

where

$$\mathbf{E}=(\mathbf{F}+\mathbf{F_v})\hat{\imath}+(\mathbf{G}+\mathbf{G_v})\hat{\jmath}. \tag{59}$$

This expression ''integrates'' for each ij cell to

$$\frac{\partial \mathbf{U}_{ij}}{\partial t}+\frac{1}{V_{ij}}[(\mathbf{E}\cdot\mathbf{S})_{i+1/2,j}-(\mathbf{E}\cdot\mathbf{S})_{i-1/2,j}+(\mathbf{E}\cdot\mathbf{S})_{i,j+1/2}-(\mathbf{E}\cdot\mathbf{S})_{i,j-1/2}]=\mathbf{W}_{ij}. \tag{60}$$

Viscous fluxes are discretized via central difference approximation. The inviscid fluxes are solved via a second-order TVD formulation using characteristic variable extrapolation with the Roe flux difference splitting Riemann solver[29,30] and the minmod limiter. In the Roe schemes, the cell-face fluxes for the flux vector $\mathbf{F}$ at the cell face $i+1/2$ may be expressed as:[31]

$$\mathbf{F}_{i+1/2}=\frac{1}{2}[\mathbf{F}(\mathbf{U}^R)+\mathbf{F}(\mathbf{U}^L)]-\frac{1}{2}\hat{\mathbf{T}}^{-1}|\hat{\Lambda}|\hat{T}(\mathbf{U}^R-\mathbf{U}^L), \tag{61}$$

where the Jacobian of $\mathbf{F}$ ($\mathbf{A}=\partial\mathbf{F}/\partial\mathbf{U}$ is expressed in terms of $\mathbf{\Lambda}$, the diagonal matrix of its eigenvalues, and $\mathbf{T}^{-1}$ and $\mathbf{T}$, the eigenvector matrices, as $\mathbf{A}=\mathbf{T}^{-1}\mathbf{\Lambda}\mathbf{T}$). The ($\hat{}$) indicates that the quantity is evaluated using the Roe averages at the $i+1/2$ face, which are based on the formulations given by Grossman *et al.*[30,32] for nonequilibrium gases. $\mathbf{U}^R$ and $\mathbf{U}^L$ are calculated from the characteristic variables, $\mathscr{W}^R$,$\mathscr{W}^L$, which are extrapolated to the cell faces using the minmod limiter defined as[33]

$$\text{minmod}(a,b)=\frac{1}{2}[\text{sgn}(a)+\text{sgn}(b)]\min(|a|,|b|). \tag{62}$$

The characteristic variables are related to the conservative variables by

$$\mathscr{W}=\mathbf{T}\mathbf{U}. \tag{63}$$

The left and right states at a given cell face are calculated using a slope limiter.[33] For cell face $i+1/2$, the right state is

$$\mathscr{W}^R=\mathscr{W}_{i+1}-\frac{1}{2}\text{minmod}[\Delta_{i+1},\Delta_i] \tag{64}$$

where

$$\mathscr{W}_{i+1}=\mathbf{T}_{i+1}\mathbf{U}_{i+1}, \tag{65}$$

$$\mathscr{W}_{i+2}=\mathbf{T}_{i+1}\mathbf{U}_{i+2}, \tag{66}$$

$$\mathscr{W}_{i}=\mathbf{T}_{i+1}\mathbf{U}_{i}, \tag{67}$$

$$\Delta_i=\mathscr{W}_{i+1}-\mathscr{W}_i. \tag{68}$$

The left is given by

$$\mathscr{W}^L=\mathscr{W}_i+\frac{1}{2}\text{minmod}[\Delta_i,\Delta_{i-1}], \tag{69}$$

where

$$\mathscr{W}_{i}=\mathbf{T}_{i}\mathbf{U}_{i}, \tag{70}$$

$$\mathscr{W}_{i+1}=\mathbf{T}_{i}\mathbf{U}_{i+1}, \tag{71}$$

$$\mathscr{W}_{i-1}=\mathbf{T}_{i}\mathbf{U}_{i-1}, \tag{72}$$

$$\Delta_i=\mathscr{W}_{i+1}-\mathscr{W}_i. \tag{73}$$

From here, the left and right conservative variable vectors, $\mathbf{U}^R=\mathbf{T}_{i+1}^{-1}\mathscr{W}^R$ and $\mathbf{U}^L=\mathbf{T}_i^{-1}\mathscr{W}^L$, respectively, can be computed for the $i+1/2$ face.

The spatial discretization above leads to a semi-discrete system of ordinary differential equations, which are solved using second- and third-order Runge–Kutta methods. Explicit time integration is suitable for hypersonic flow calculations when the source terms are not stiff. For nonequilibrium calculations, the source terms are often too stiff for explicit time integration. In this case, a class of semi-implicit Runge–Kutta schemes developed by Zhong[20] are employed. A third-order Additive Semi-Implicit Runge–Kutta scheme can be expressed as

$$[\mathbf{I}-ha_1\mathbf{J}(\mathbf{U}^n)]\mathbf{k}_1=h[\mathbf{H}(\mathbf{U}^n)+\mathbf{W}(\mathbf{U}^n)], \tag{74}$$

$$[\mathbf{I}-ha_2\mathbf{J}(\mathbf{U}^n+c_{21}\mathbf{k}_1)]\mathbf{k}_2=h[\mathbf{H}(\mathbf{U}^n+b_{21}\mathbf{k}_1)+\mathbf{W}(\mathbf{U}^n+c_{21}\mathbf{k}_1)], \tag{75}$$

$$[\mathbf{I}-ha_3\mathbf{J}(\mathbf{U}^n+c_{31}\mathbf{k}_1+c_{32}\mathbf{k}_2)]\mathbf{k}_3=h[\mathbf{H}(\mathbf{U}^n+b_{31}\mathbf{k}_1+b_{32}\mathbf{k}_2)+\mathbf{W}(\mathbf{U}^n+c_{31}\mathbf{k}_1+c_{32}\mathbf{k}_2)], \tag{76}$$

$$\mathbf{U}^{n+1}=\mathbf{U}^n+\omega_1\mathbf{k}_1+\omega_2\mathbf{k}_2+\omega_3\mathbf{k}_3, \tag{77}$$

where $\mathbf{U}^n$ is the vector of conserved quantities at step n, $\mathbf{H}$ is terms obtained in the semi-discrete formula resulting from the conservative flux vectors, $\mathbf{W}$ is the stiff source term vector, $\mathbf{J}=\partial\mathbf{W}/\partial\mathbf{U}$ is the Jacobian matrix of the source term, and h is the time step. The coefficients derived by Zhong are[20]

$$\begin{array}{ll}\omega_1=1/8, & \omega_2=1/8,\\ \omega_3=3/4, & b_{21}=8/7,\\ b_{31}=71/252, & b_{32}=7/36,\\ a_1=0.797097, & a_2=0.591381,\\ a_3=0.134705, & c_{21}=1.05893,\\ c_{31}=1/2, & c_{32}=-0.375939.\end{array}$$

The time stepping algorithm independent of the nonequilibrium model has been tested by calculating a pseudo-steady Mach reflection, where the numerical solutions were compared with available experimental and numerical results. Good agreement between the current code and experiment was obtained. Detailed results of this were previously presented in Ref. 34.

IV. STEADY HYPERSONIC FLOW PAST A CYLINDER

To validate the nonequilibrium capability of the code and to test two different chemistry models, hypervelocity flow past cylinders based on published experimental data was computed. The first case was based on an experiment by Hornung.[35] The case was flow past a 1 in. diameter cylinder with $u_\infty=5590$, m/s $T_\infty=1833$ K, $p_\infty=2910$ Pa, and a Reynolds number of 6000. The gas in the freestream was partially dissociated nitrogen, 92.7% N_2 and 7.3% N by mass. The flow conditions match those studied experimentally by Hornung and computationally by Candler.[11] Two chemistry models were tested for this case. The first was the Dunn–Kang rate coefficient model,[25] and the second was the popu-

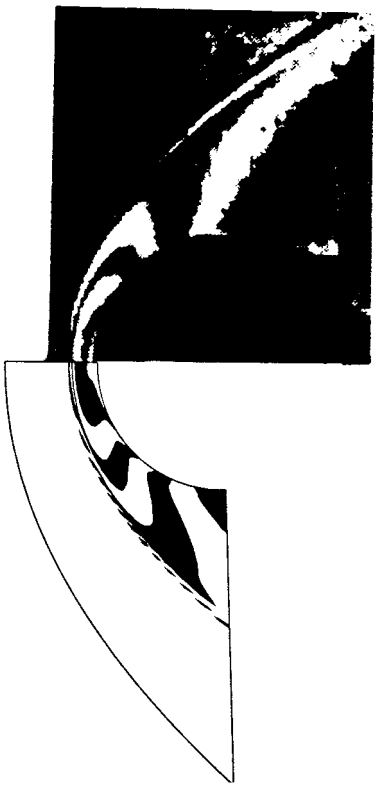

FIG. 4. Computational interferogram using the Dunn–Kang model (bottom) compared with experimental results of Hornung (top) for hypervelocity flow over a cylinder.

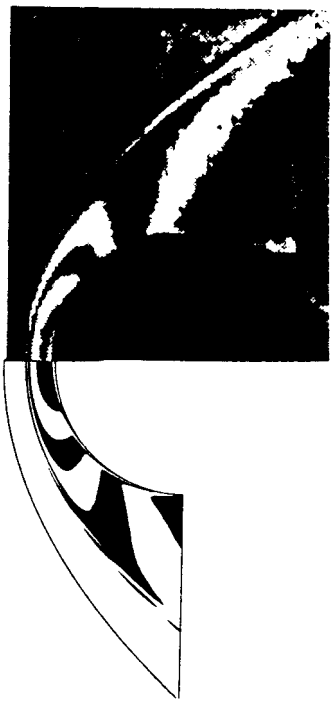

FIG. 5. Computational interferogram using the Park model (bottom) compared with experimental results of Hornung (top) for hypervelocity flow over a cylinder.

lar Park model.[19] Figures 4 and 5 present computed interferograms compared with experimental interferograms from Hornung.[35]

Reasonable agreement was attained for flow structure. Figure 4 compares the present computation with the Dunn–Kang model to the experiments of Hornung. Good agreement between computation and experiment for shock shape and stand off distance has been obtained. Flow structure, however does show noticeable differences. The authors feel this is due to both inaccuracies in the models used and the incomplete knowledge of the internal thermal modes of the freestream.

Figure 5 compares the present computation with the Park model to the experiments of Hornung. Good agreement between computation and experiment for shock shape and stand off distance has been obtained. Flow structure, however does show noticeable differences, most notably along the stagnation line.

As a comparison between the two chemistry models, Figure 6 presents fringe number profiles along the stagnation line for both models along with experimental data taken from Ref. 35. The Park model yielded better results than did the Dunn–Kang model. Additionally, both models tended to yield results closer to an equilibrium solution than demonstrated by experiment. While the Park model produced marginally better results than the Dunn–Kang model and will be used in future work, the present study primarily uses the Dunn–Kang model. The Dunn–Kang model is computationally more efficient,[36] and was the model originally in the code when this study began.

The second case was based on an experiment by Sanderson[15] in the T5 shock tunnel at Caltech. The case was flow past a 4.06 cm diameter cylinder with $u_\infty = 4450$ m/s, $\rho_\infty = 0.0155$ kg/m^3, $p_\infty = 5480$ Pa. The gas in the freestream

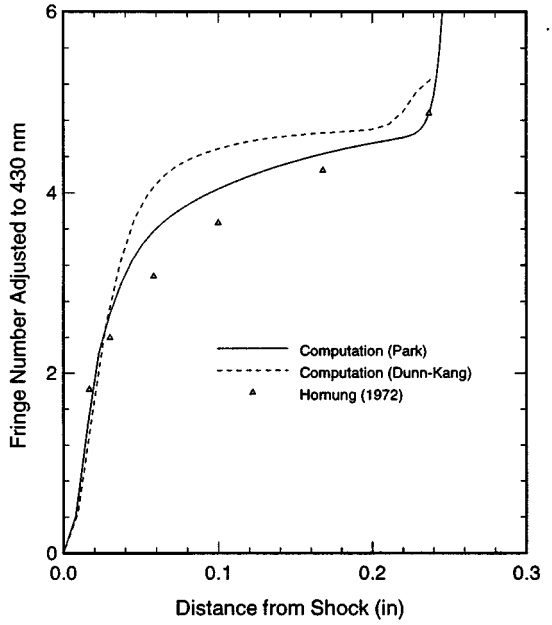

FIG. 6. Computed fringe numbers for the two chemistry models compared with experimental values of Hornung along a stagnation line.

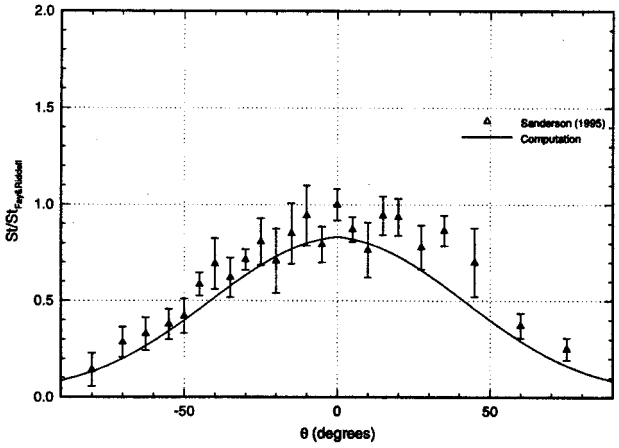

FIG. 7. Computed surface Stanton number ($St = \dot{q}/\rho_\infty u_\infty h^\circ_\infty$) profiles compared with the experimental data of Sanderson.

was partially dissociated nitrogen, 99.034% N_2 and 0.966% N by mass. Figure 7 presents surface Stanton number ($\dot{q}/\rho_\infty u_\infty h^\circ_\infty$) profiles, normalized by the theoretical stagnation point Stanton number,[15] for both the present computations and Sanderson's experiment. Reasonable agreement between experiment and computation was obtained.

A computed interferogram compared with the published experimental interferogram is presented in Fig. 8. The interference fringes behind the shock agree well with experiment. The present code computed a fringe shift at the boundary layer edge near the stagnation point of 10.76 while Sanderson reported a measured fringe shift of 10.5. However, shock stand off distance for this case was not in as good agreement with experiment as it was for Hornung's case. The differences between computation and Sanderson's experiment are, as yet, unexplained. However, a recent work by Olejniczak *et al.*[37] comparing computational results to double wedge experiments in T5 indicates that the freestream of the test section is not in thermal equilibrium. Because data on the thermal internal states of the freestream for the cylinder experiment was not available, the present paper assumed a thermal equilibrium freestream. The effect of this assumption in light of the recent work in Ref. 37 will be examined in the near future.

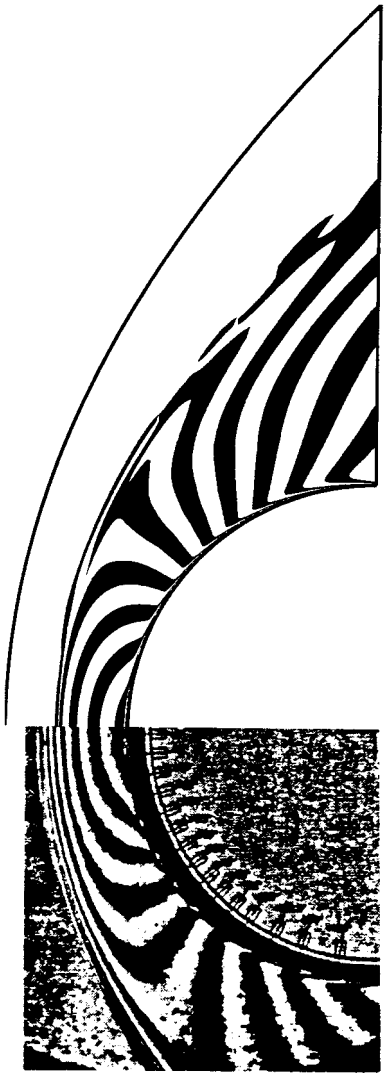

FIG. 8. Computed interferogram (top) compared with the experimental data of Sanderson (bottom).

V. STEADY SHOCK/BOUNDARY LAYER INTERACTION WITH REAL-GAS EFFECTS

A steady shock/boundary layer interaction on a flat plate was studied for hypersonic flow with nonequilibrium real-gas effects. A schematic of this flow field is shown in Fig. 2. The effects of both thermo-chemical nonequilibrium and freestream enthalpy were investigated by numerical simulations.

The following flow conditions were used in the investigation. The flow deflection angle across the incident shock was 22°, the freestream Mach number was 7.0, the gas was air with a freestream composition of 79% N_2 and 21% O_2 by mass, the Reynolds Number, based on freestream values and the shock impingement distance from the leading edge, was 3.571×10^5, and the shock impingement distance from the leading edge was 0.2134 m. No slip and isothermal wall boundary conditions were used on the plate surface. The wall temperature was 1200 K. An 88 by 72 (x by y) Cartesian grid, exponentially stretched in the y direction, was used. The simulations were run to steady-state at a CFL number of 0.3.

A. Effects of thermal and chemical nonequilibrium

In the numerical computations, the steady flow fields of the shock/boundary layer interaction were computed using three physical models with different levels of excitation of internal modes. The first model assumed the gas is perfect (ideal) gas with frozen vibrational modes and frozen chemical modes (no dissociation/recombination). The second model assumed the diatomic molecules were vibrationally excited but chemically frozen. The third model assumed the gas was both vibrationally and chemically excited (reacting). The nonequilibrium real-gas effects on steady shock/boundary layer interaction were studied by comparing the

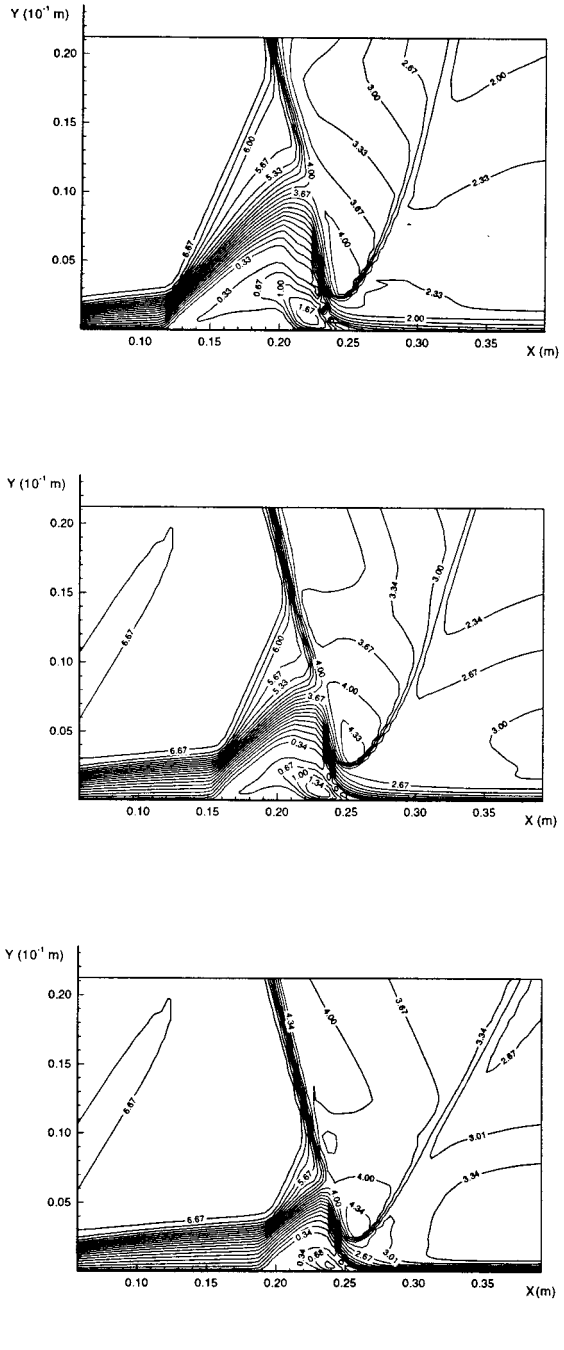

FIG. 9. Mach number contours for shock/boundary layer interaction with different physical models: (a) ideal gas, (b) vibrational excitation and frozen chemistry, (c) full nonequilibrium gas ($T_\infty = 1600$ K, $M_\infty = 7$). The y axis has been magnified by a factor of 10 relative to the x axis for clarity.

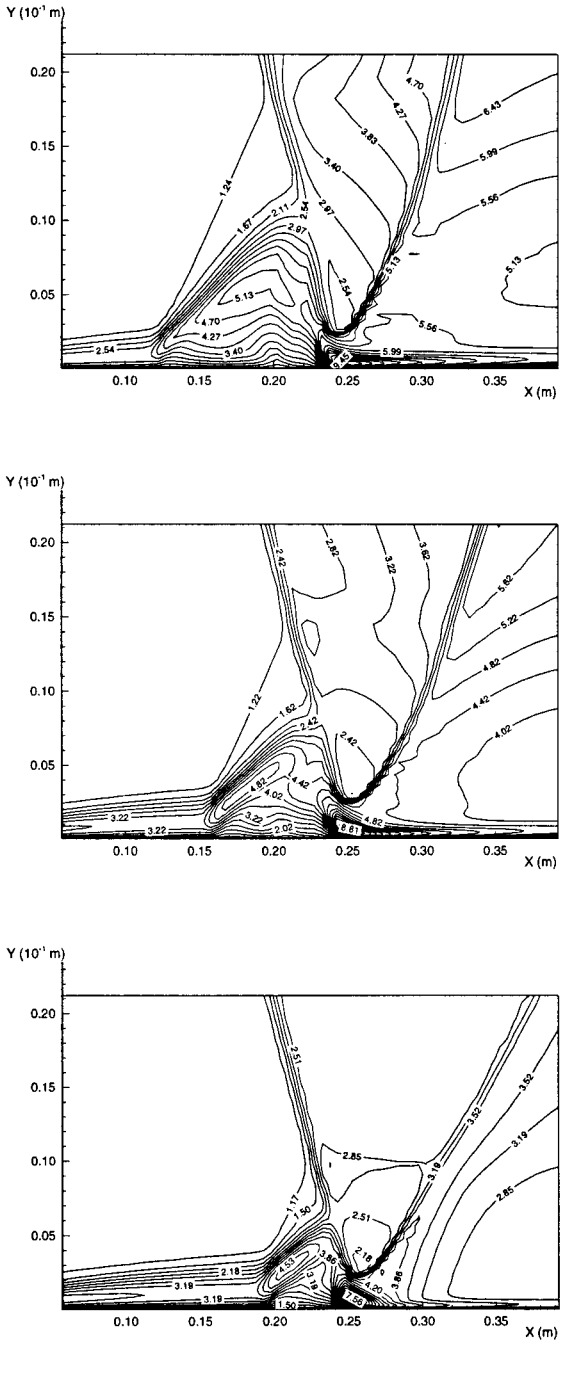

FIG. 10. Translational temperature (K) contours for shock/boundary layer interaction with different physical models: (a) ideal gas, (b) vibrational excitation and frozen chemistry, (c) full nonequilibrium gas ($T_\infty = 1600$ K, $M_\infty = 7$). The y axis has been magnified by a factor of 10 relative to the x axis for clarity.

numerical results of these three perfect (ideal), vibrationally excited but chemically frozen, and nonequilibrium (reacting) models.

Figures 9 and 10 show the Mach number contours and the translational temperature contours for the solutions of shock interaction using the three different gas models. The translational temperature contours are normalized by the freestream temperature. The freestream temperature and density of the test case was 1600 K and 0.0169 kg/m^3, respectively. The y-axis in the contours has been magnified by a factor of 10 in order to show the region around the shock impingement point. The contours show clearly the incident shock impinging on the wall and a separation bubble ahead of the shock impingement point. The reflected shock can be seen in each picture where the separated flow reattaches behind the separation bubble. The figures show that the nonequilibrium gas effects reduce size of the separation bubble

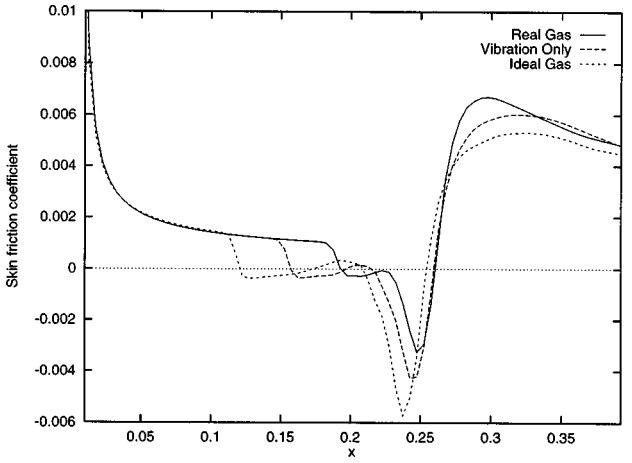

FIG. 11. Skin friction coefficient c_f distribution along the flat plate for the three gas models.

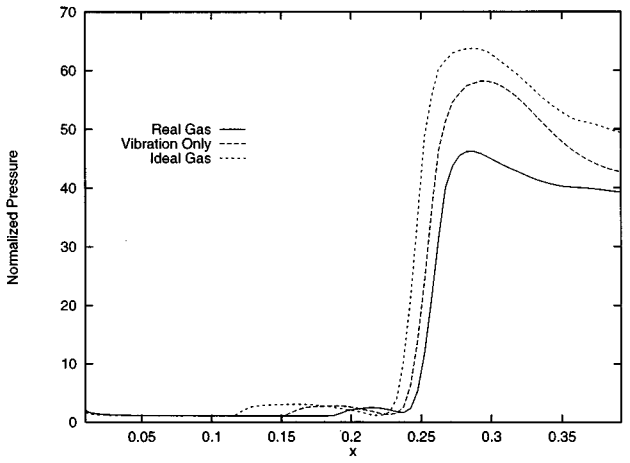

FIG. 12. Normalized pressure p/p_∞ distribution along the flat plate for the three gas models.

in the flow field. The separation region is largest in Fig. 9(a) for the ideal gas model, decreases in size in Fig. 9(b) for the vibrational nonequilibrium model, and is smallest in Fig. 9(c) for the thermo-chemical nonequilibrium model. To quantify this change, bubble size was nondimensionalized using the distance from the leading edge the shock would impinge at for the perfect inviscid gas case. The effects on separation bubble size were as follows:

Model	Bubble size;
Ideal gas	0.4920;
Vibration nonequilibrium only	0.4218;
Thermo-chemical nonequilibrium	0.3046.

The temperature contours in the ideal [Fig. 10(a)], chemically frozen [Fig. 10(b)], and reacting [Fig. 10(c)] cases also show that the peak temperature in the shock impingement region were highest for the ideal case and lowest for the reacting case. The temperatures in the boundary layer behind the impinging shock were found to be about 9500 K for the ideal case, 7700 K for the chemically frozen case, and 6700 K for the reacting case.

The temperature reduction due the nonequilibrium effects is expected to lead to less heating rates on the surface. These effects can be seen in the surface distribution of aerodynamic properties. Figures 11, 12, and 13 are the distribution of the skin friction coefficient ($\tau_{xy}/1/2\,\rho_\infty u_\infty^2$), normalized pressure ($p/p_\infty$), and heating rates along the surface for the three gas models. The surface skin friction (Fig. 11) shows that nonequilibrium effects reduce the size of the separation region and the magnitude of skin friction inside the bubble. These effects can also be seen in the surface pressure profiles (Fig. 12) where the ideal case exhibited the largest pressure jump, while the reacting case showed the lowest jump. In the surface heat transfer profiles given in Fig. 13, the ideal case resulted in the highest heating rate to the wall in the shock impingement region while the lowest heating rate was given by the reacting case.

The decrease in temperature and bubble size of the nonequilibrium cases is due to the endothermic nonequilibrium effects. Between the ideal and vibrational nonequilibrium cases, the energy is distributed among more internal modes in the nonequilibrium case, resulting in a lower thermodynamic temperature in the latter case. Similarly, dissociation reactions are endothermic, absorbing energy from the flow to break the chemical bonds. This reduces the temperature and pressure of the gas in the thermo-chemical nonequilibrium case. This pressure reduction results in a less severe adverse pressure gradient and a smaller separation bubble. The lower flow temperature near the isothermal wall for the reacting case results in smaller temperature gradients and lower heat transfers rates relative to the ideal and chemically frozen cases.

B. Effects of freestream enthalpy

The nonequilibrium effects are a result of the high enthalpy level in the freestream. Four test cases with different level of freestream enthalpy were computed to investigate the effect of freestream enthalpy on the results of the nonequilibrium thermo-chemical model. The flow conditions of

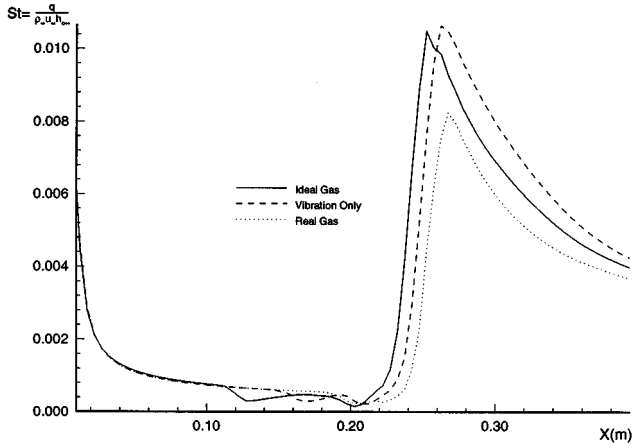

FIG. 13. Normalized heat flux $\dot{q}/\rho_\infty u_\infty h_\infty^\circ$ distribution along the flat plate for the three gas models.

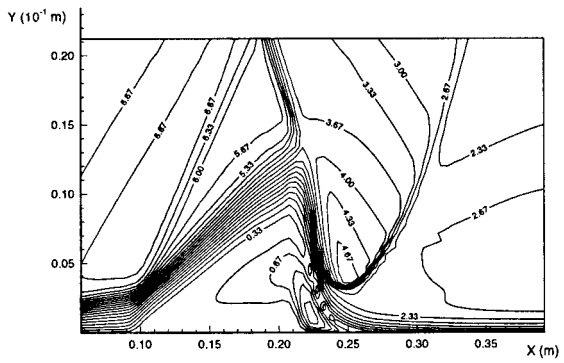

(a)

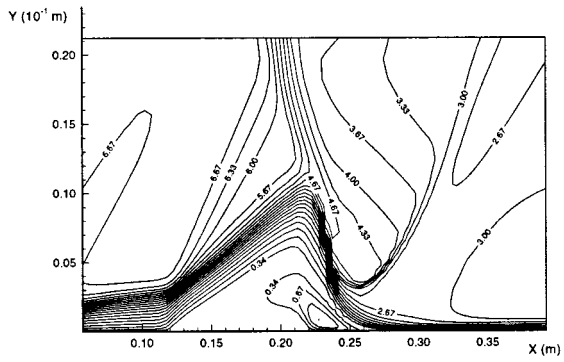

(b)

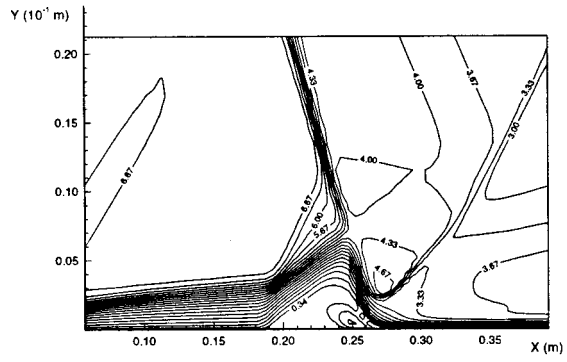

(c)

FIG. 14. Mach number contours for Mach 7 shock/boundary layer interaction with the full nonequilibrium model at different freestream enthalpies: (a) $T_\infty = 700$ K, (b)$T_\infty = 1200$ K, (c) $T_\infty = 2000$ K. The y axis has been magnified by a factor of 10 relative to the x axis for clarity.

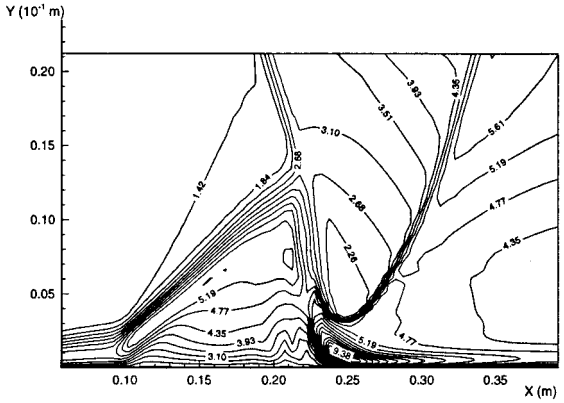

(a)

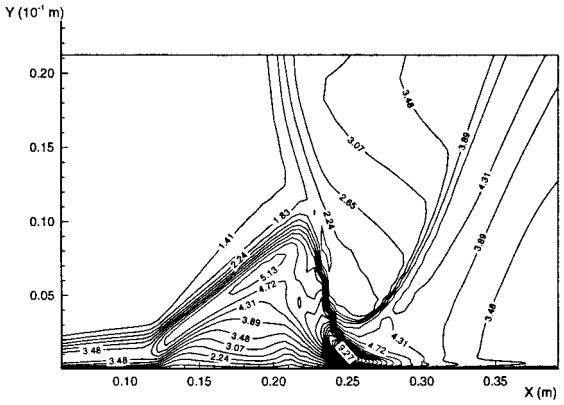

(b)

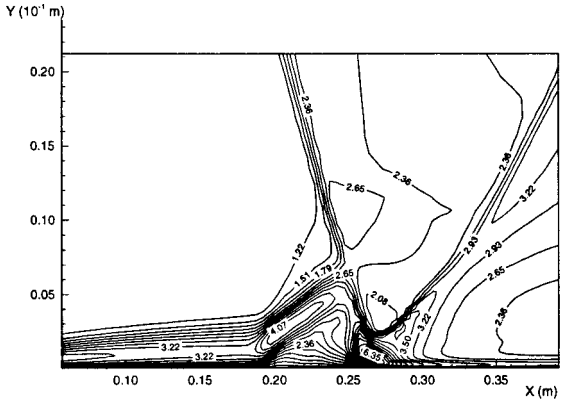

(c)

FIG. 15. Translational temperature (T_t/T_∞) contours for Mach 7 shock/boundary layer interaction with the full nonequilibrium model at different freestream enthalpies: (a) $T_\infty = 700$ K, (b) $T_\infty = 1200$ K, (c) $T_\infty = 2000$ K. The y axis has been magnified by a factor of 10 relative to the x axis for clarity.

the four test cases were the same as those of the previous cases except the following freestream temperature and density. Case 1 $T_\infty = 700$ K, $\rho_\infty = 0.0140$ kg/m^3; Case 2 1200 K, 0.0158 kg/m^3; Case 3 1600 K, 0.0169 kg/m^3; Case 4 2000 K, 0.0178 kg/m^3. Among the four cases, the results of case 3 have been presented in the previous section.

The Mach number and translational temperature contours of the nonequilibrium reacting models for test case 1, 2, and 4 are shown in Fig. 14 and Fig. 15. Again, the temperature contours are normalized by the freestream temperature, and the y-axis is magnified by a factor of 10 for clarity. Figures 16, 17, and 18 compare the distribution of skin friction coefficient, normalized pressure, and species mass fractions along the surface among the results of different freestream enthalpy. As the freestream temperature increases, the contours show that the separation bubble decreases in size in general. However, for the highest temperature case, Case 4, this trend reverses. The effects of

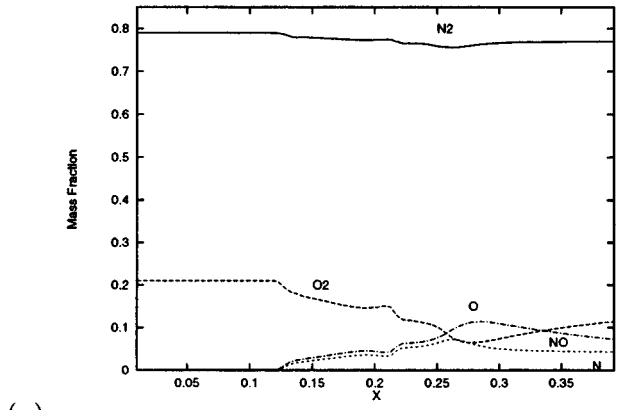

(a)

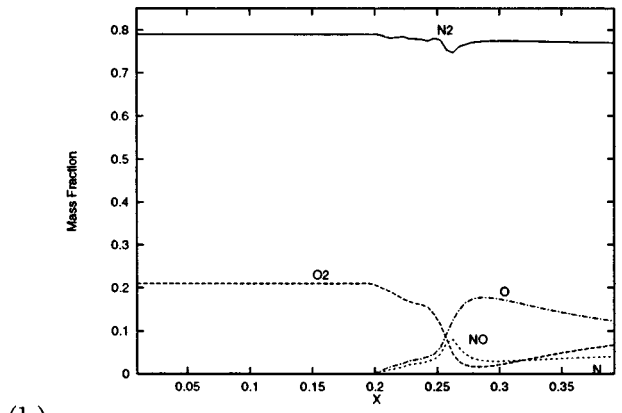

(b)

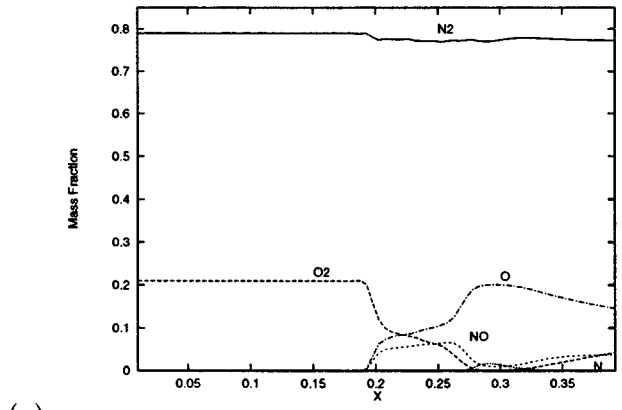

(c)

FIG. 16. Species mass fractions along the wall for the Mach 7 shock/boundary layer interaction with the full nonequilibrium model at different freestream enthalpies: (a) $T_\infty = 1200$ K, (b) $T_\infty = 1600$ K, (c) $T_\infty = 2000$ K.

freestream enthalpy on flow properties are examined by comparing the flow property distribution along the surface. From the skin friction (Fig. 17), the normalized the separation bubble sizes for the four test cases are the following: Case 1 $T_\infty = 700$ K, bubble size=0.539; Case 2 1200 K, 0.422; Case 3 1600 K, 0.305; Case 4 2000 K, 0.374. There is

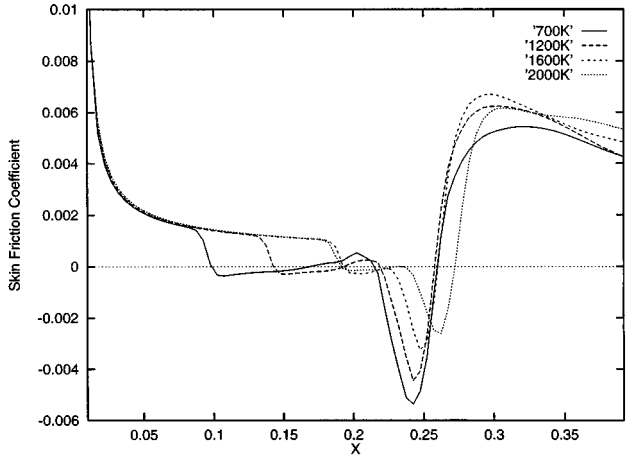

FIG. 17. Skin friction coefficient c_f distribution along the flat plate for different freestream temperatures.

a difference in flow structure between Case 4 and the other three cases, which can be seen by examining the surface pressure profiles in Fig. 18. The pressure profiles for the 700 K, 1200 K, and 1600 K cases all peak just after the shock impingement point, and gradually relax to a lower value. The 2000 K case, however, has a secondary pressure rise following the initial rise due to the impinging shock. This is due to the fact that N_2 has a higher dissociation temperature than O_2. In the surface mass fraction profiles shown in Figs. 16(a) and 16(b), no significant amounts of atomic nitrogen were observed. However, in the $T=2000$ K case, temperatures became high enough so that nitrogen dissociation occurred in measurable quantities, as seen at $x=0.3$ in Fig. 16(c), and changed the flow field. This nitrogen dissociation region corresponds to where the pressure profile for Case 4 in Fig. 18 departs from the trends of the other three cases. Instead of a pressure drop as the oxygen recombines to equilibrium values, the pressure for the $T=2000$ K case continues to increase, extending the separation region.

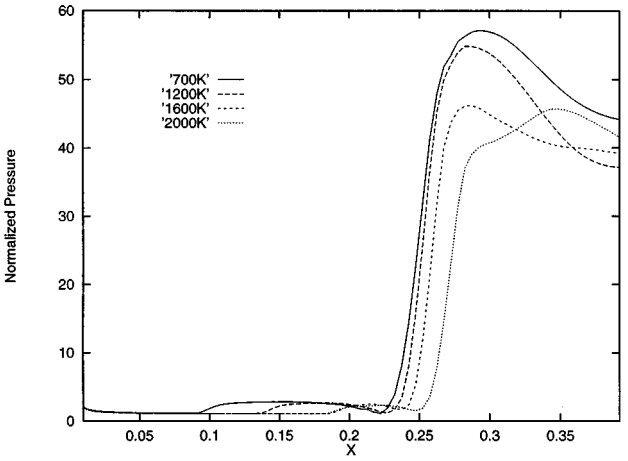

FIG. 18. Normalized pressure p/p_∞ distribution along the flat plate for different freestream temperatures.

The surface mass fraction profiles in Fig. 16 also show that the point at which dissociation begins is coincident with the front edge of the separation bubble. This occurs at $x=0.12$ for Case 2, as seen by comparing Figs. 15(b) and 16(a), and at $x=0.19$ for Cases 3 and 4, as seen by comparing Figs. 10(c) with 16(b) and Figs. 15(c) with 16(c). In addition, the skin friction coefficients reduce as the freestream enthalpy increases because of the endothermic nonequilibrium real-gas effects.

The present results indicate that real-gas effects significantly influence the structure of hypervelocity shock/boundary layer interactions. In the test cases studied in this paper, the presence of real-gas effects decreased the size of the shock induced separation region relative to the perfect gas case. Also, the post impingement surface heating rates were significantly reduced by the endothermic relaxation of the internal and chemical modes. The direction of the influence of real-gas effects is dependent on the endothermic or exothermic nature of the nonequilibrium processes. Earlier work done by Ballaro and Anderson,[12] and Grumet *et al.*[13] indicated that real-gas effects could increase the heating rates. However, in those studies, the dominating reactions near the wall were recombination reactions, which are exothermic, while in the present case, the dominating reactions were dissociation reactions, which are endothermic.

VI. UNSTEADY TYPE IV SHOCK INTERFERENCE HEATING WITH REAL-GAS EFFECTS

A two-dimensional unsteady type IV interference heating problem with real-gas was studied by time-accurate numerical simulations of the Navier–Stokes equations with the nonequilibrium gas model. Time accurate calculations were performed using the third-order Additive Semi-implicit Runge–Kutta scheme. Because the type IV interference heating problems are inherently unsteady, the calculations were run until a sustained oscillation in the maximum surface pressure was obtained to ensure all transients had died out. The numerical solutions of the type IV interaction with real-gas effects were first checked against simple analysis for shock interaction with equilibrium gas models. The real-gas effects on unsteady interference heating problems were then numerically studied.

The flow conditions of the test case was based on an ideal-gas case studied in Refs. 4 and 38. In order to investigate the effect of thermo-chemical nonequilibrium, the original freestream conditions were altered so that dissociation would occur behind the bow shock. The new freestream was an undissociated N_2 flow with the following conditions:

Cylinder radius	$=0.0381$ m;
Flow deflection (impinging shock)	$=12°$;
Re	$=2.57354\times105$;
M_∞	$=8.03$;
P_∞	$=985.015$ Pa;
T_∞	$=800$ K;
T_{wall}	$=1000$ K.

Under these conditions, the impinging shock wave was weak enough so that the flow behind it was an undissociated equilibrium gas. But the temperature behind the bow shock is strong enough to produce dissociation and recombination. The results presented in this paper were obtained using a 194 by 124 stretched body-fitted grids such as the one shown in Fig. 19.

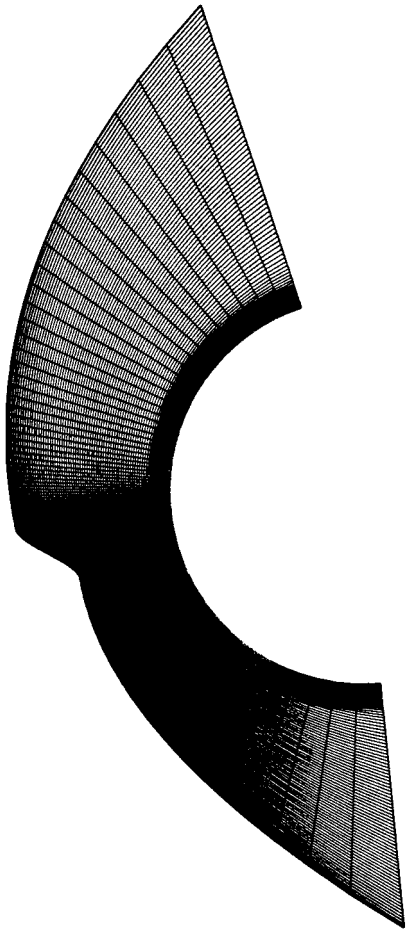

FIG. 19. An example of the grid used in Type IV shock–shock interference heating computations. The grid shown is coarser than the actual one for clarity.

A. Accuracy estimate of the numerical results

The numerical accuracy of results presented below were estimated by a grid refinement study. Computations of undisturbed flow over a cylinder with the same freestream conditions as those listed above were carried out using two grids of differing densities. Using the Richardson extrapolation technique for second-order accurate schemes, the maximum numerical errors of the current results were estimated to be 3.3% for heat transfer and 0.067% for pressure. The greater errors in heat transfer than in pressure is due to the fact that heat fluxes are viscous effects dependent on temperature gradients which are more sensitive to grid spacing. On the other hand, pressure is mainly due to inviscid effects and is relatively insensitive to grid spacing.

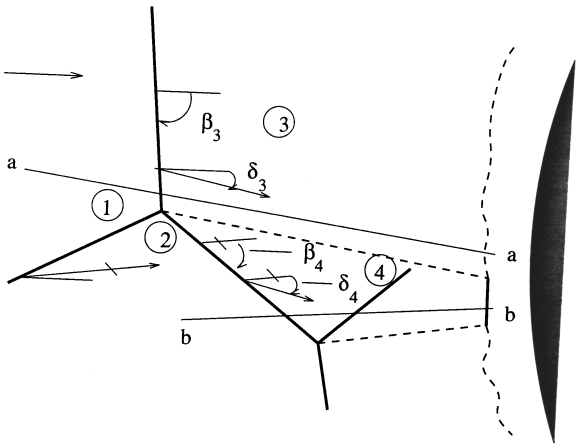

FIG. 20. Schematic of shock interaction solved by analytical analysis. Lines a–a and b–b indicate lines along which comparison of numerical and analytical solutions were made.

B. Analytical models for shock interaction for equilibrium flow

As a validating check on the computations, numerical results were compared with analytical predictions for flow variables in thermo-chemical equilibrium behind the interacting shocks. Flow conditions across the shock interaction point were solved using an iterative technique for shock jump conditions with an equilibrium real-gas model behind the shock. The gas model behind the shock was the ideal dissociating gas model of Lighthill,[21] in conjunction with the hydrodynamic jump conditions across the shock waves. The procedure was similar to that used by Sanderson[15] in his analysis of experimental data.

The flow field was divided into four regions as shown in Fig. 20. In the figure, region 1 is the freestream, region 2 is the flow behind the impinging shock, region 3 is the area behind the upper bow shock, and region 4 is the jet region behind the shock transmitted due to the oblique shock impingement. Hydrodynamic jump relations are given by

$$p_3-p_1=\rho_1 u_1^2\sin^2(\beta_3)\left(1-\frac{\rho_1}{\rho_3}\right), \tag{78}$$

$$\rho_1 u_1\sin(\beta_3)=\rho_3 u_3\sin(\beta_3-\delta_3), \tag{79}$$

$$h_1+\frac{1}{2}u_1^2\sin^2(\beta_3)=h_3+\frac{1}{2}u_3^2\sin^2(\beta_3-\delta_3), \tag{80}$$

$$u_1\cos(\beta_3)=u_3\cos(\beta_3-\delta_3), \tag{81}$$

$$p_4-p_2=\rho_4 u_4^2\sin^2(\beta_4)\left(1-\frac{\rho_2}{\rho_4}\right), \tag{82}$$

$$\rho_2 u_2\sin(\beta_4)=\rho_4 u_4\sin(\beta_4-\delta_4), \tag{83}$$

$$h_2+\frac{1}{2}u_2^2\sin^2(\beta_4)=h_4+\frac{1}{2}u_4^2\sin^2(\beta_4-\delta_4), \tag{84}$$

$$u_2\cos(\beta_4)=u_4\cos(\beta_4-\delta_4), \tag{85}$$

together with the equations of state,

$$p_3=\rho_3(1+\alpha_3)R_{N_2}T_3, \tag{86}$$

$$p_4=\rho_4(1+\alpha_4)R_{N_2}T_4. \tag{87}$$

These jump equations were simultaneously solved across the shocks dividing regions 1 and 3 and dividing regions 2 and 4. In the above equations, β_3 and β_4 are the angles shocks 3 and 4 make with the incident stream, δ_3 and δ_4 are the flow deflections in regions 3 and 4 with respect to the incident streams. This is shown schematically in Fig. 20. R_{N_2} is the gas constant for nitrogen, α is the mass fraction of atomic nitrogen in the region indicated by the subscript. The enthalpy, h, can be expressed as

$$h=\frac{7}{2}R_{\mathrm{N}_2}T+\frac{\theta_v R_{\mathrm{N}_2}}{\exp(\theta_v/T)-1}+\alpha\left(\frac{3}{2}R_{\mathrm{N}_2}T-\frac{\theta_v R_{\mathrm{N}_2}}{\exp(\theta_v/T)-1}+h_{\mathrm{N}}^{\circ}\right), \tag{88}$$

where h_{N}° is the heat of formation of atomic nitrogen.

The gas in regions 3 and 4 was assumed to be in thermo-chemical equilibrium governed by the Lighthill ideal dissociating gas model:

$$\frac{\alpha_3^2}{1-\alpha_3}=\frac{\rho_3}{\rho_d}e^{-\theta_d/T_3}, \tag{89}$$

$$\frac{\alpha_4^2}{1-\alpha_4}=\frac{\rho_4}{\rho_d}e^{-\theta_d/T_4}, \tag{90}$$

where θ_d and ρ_d are parameters characterizing the dissociation reaction and can be found in Vincenti and Kruger[21] as $\theta_d=113{,}100$ K and $\rho_d=130$ g/cm^3 for nitrogen.

The equations for flow variables in regions 3 and 4 are closed by pressure and flow direction continuity equations across the slip line dividing regions 3 and 4. The values in regions 1 and 2 were taken as known values given by the boundary conditions of the problem. The solution to the above system of equations was obtained via an iterative method.

Figure 21 shows a comparison of numerical and analytic solutions for pressure in region 3 and region 4. The upper figure shows a profile along line a–a in Fig. 20, while the lower figure shows a profile along line b–b. The computed values for pressure match well with the analytical values. The slight discrepancy in the results are expected because the analytic solution assumed thermo-chemical equilibrium, and uniform flow in regions 3 and 4 with no viscous dissipation at the interface. Because analytical solutions for two-dimensional viscous real-gas interaction problems were not available, numerical solutions were used to study the real-gas effects on the interference heating phenomena.

C. Unsteady mechanism

Numerical calculations showed that the type IV flow field of this case was inherently unsteady. Instantaneous flow field contours are shown in Figs. 22–25. Figure 22 shows the instantaneous translational temperature contours. The highest temperatures in the flow field are located near the jet impingement point and behind the strong bow shocks. Behind the bow shocks, the gradual temperature decrease due to

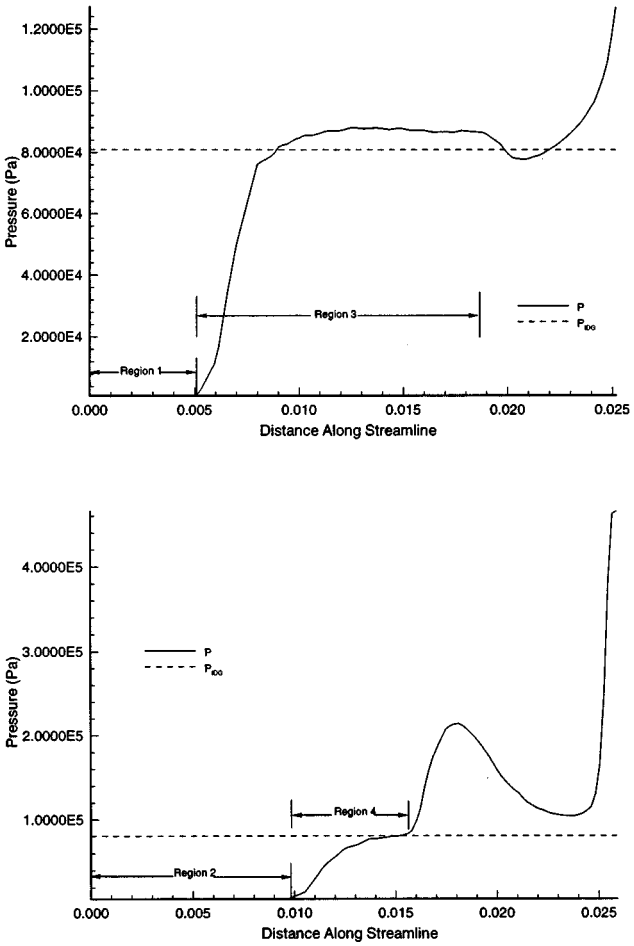

FIG. 21. Comparison of numerical and analytical results for shock–shock interaction with real-gas effects. Dashed lines indicate analytic solutions in region 3 (upper figure) and region 4 (lower figure).

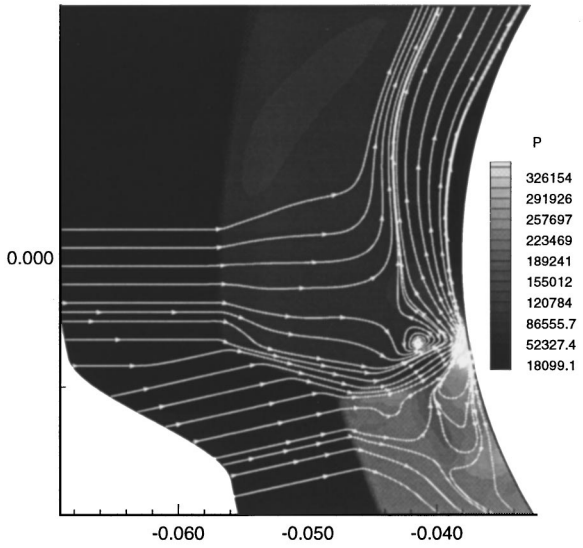

FIG. 23. Instantaneous pressure contours and streamlines of the type IV shock–shock interference heating flow.

thermal relaxation is noticeable. Figure 23 shows instantaneous streamlines and pressure contours. Vortices both above and below the supersonic jet near the jet–wall juncture are evident. These vortices play an important role in the unsteadiness of the jet, as will be discussed later. The region of maximum pressure occurs near the point where the jet impinges the wall. Figure 24 shows vibrational energy contours. The distinct differences between the values and shapes of the vibrational temperature contours and the translational temperature contours in Fig. 22 demonstrates the degree of thermal nonequilibrium present in the flow. In general, the post shock vibrational temperature is lower than the corresponding translational temperature. Figure 25 shows contours of dissociated nitrogen mass fractions. It can be seen that the supersonic jet is essentially frozen. Just behind the bow shocks, the flow is frozen, but eventually dissociates as

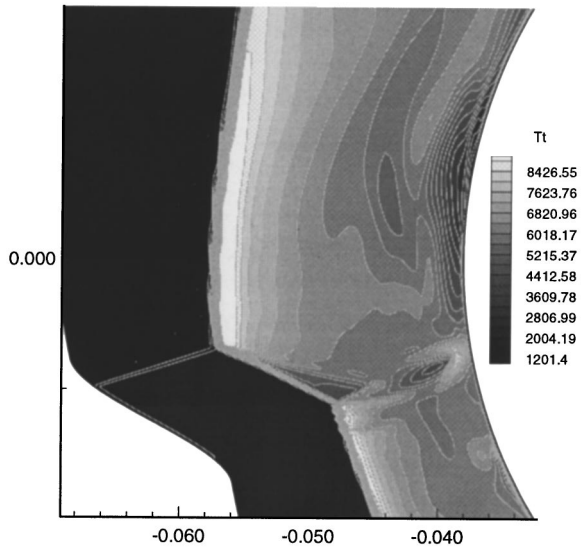

FIG. 22. Instantaneous translational temperature contours of the type IV shock–shock interference heating flow.

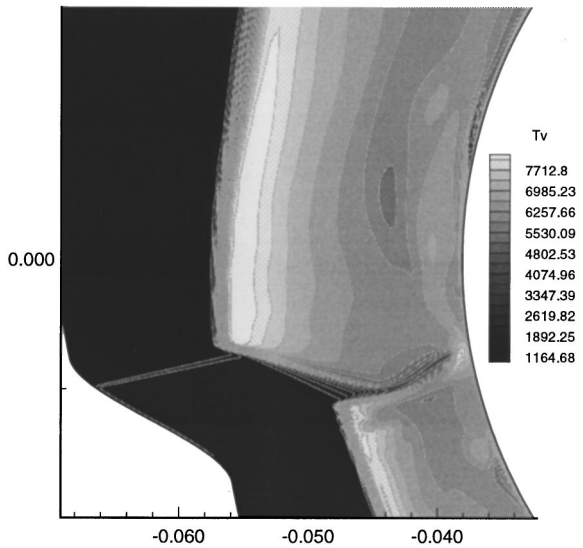

FIG. 24. Instantaneous vibrational temperature contours of the type IV shock–shock interference heating flow.

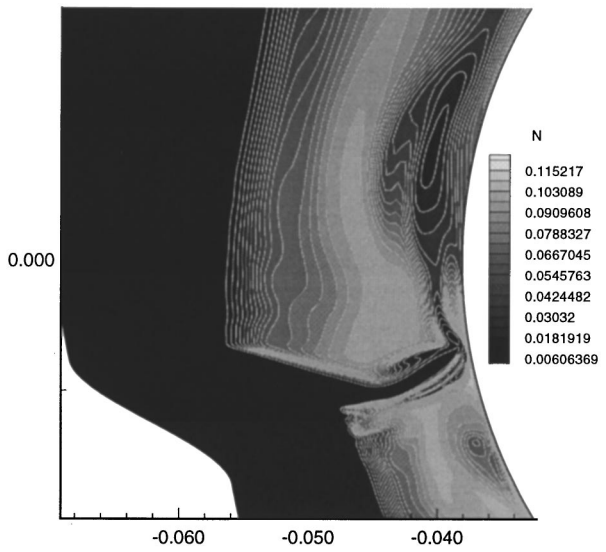

FIG. 25. Instantaneous N mass fraction contours of the type IV shock–shock interference heating flow.

it relaxes towards equilibrium. The highest concentrations of N were found near the jet impingement region.

A segment of the time history of the maximum surface pressure is shown in Fig. 26. The frame label on the curve correspond to the frame references used throughout this section. Surface heat flux profiles, normalized by the undisturbed stagnation point heat flux, for the frame references are given in Fig. 27. The large variation in peak heating rate magnitude can be seen by comparing the curves labeled frame 5, the profile with the smallest peak heating rate, and frame 21, the profile with the largest peak heating rate. The peak heating of frame 21 is about twice as large as that of frame 5. Relative to an undisturbed flow, the shock interference increases the peak surface heating by a factor of about 17.5. Pressure profiles, normalized by the undisturbed stagnation point pressure, are given in Fig. 28. Relative to an undisturbed flow, the peak surface pressure is increased by a factor of about 9.65.

Instantaneous N mass fraction contours a time sequence are shown in Fig. 29. Corresponding stream line traces and pressure contours are in Fig. 30. The oscillation of the supersonic jet can be seen by tracing the mass fraction contours along their time history. The jet is initially curved upwards, as can be seen in Fig. 29(a). The jet moves downwards until it is aligned nearly normal to the body surface in Fig. 29(b). At this point, the peak surface pressure and heating rates are at a maximum. This point is also important as it marks a change in direction of the jet motion. After this, the jet moves upwards again in Fig. 29(c) and continues to turn upwards along the body until a pressure and heating minimum is reached [Fig. 29(d) is close to this minimum point]. The mechanism behind this oscillation is related to the relative orientation of the jet to the body, and the shear layers produced along the surface which in turn create vortices which are shed into the flow.

Lind[7] found that ideal gas vortices were shed from the jet–body juncture during the course of the jet oscillations and convected off with flow, eventually dissipating in the shear layer. He proposed the vortex shedding as the cause for the unsteadiness in the flow field. The real-gas flow fields presented here also show a time dependent shedding of vortices. However, unlike Lind's case, the present case shows vortices being shed from both the upper and lower surfaces

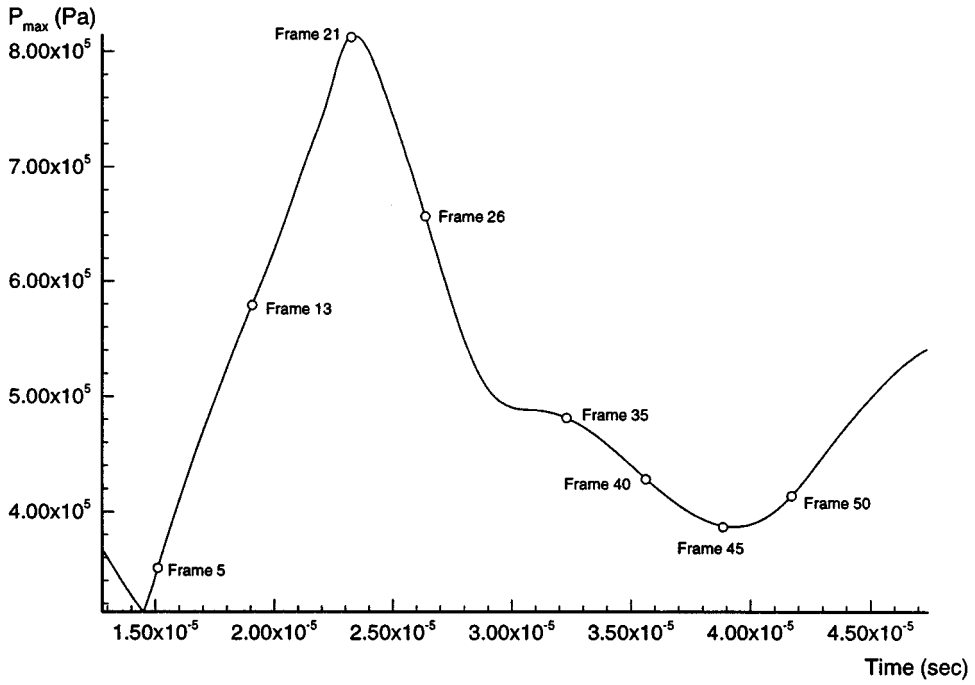

FIG. 26. Maximum surface pressure (Pa) time history for the type IV interaction.

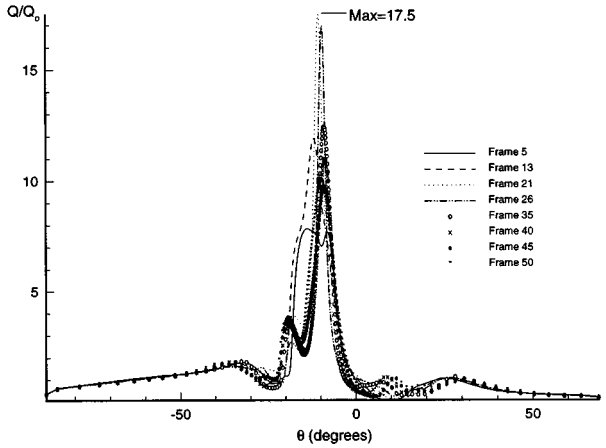

FIG. 27. Surface heat transfer profiles, normalized by undisturbed stagnation heating rates, at various times.

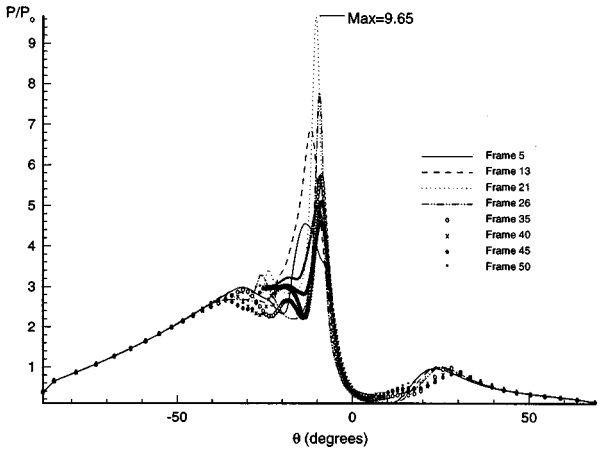

FIG. 28. Surface pressure profiles, normalized by undisturbed stagnation point pressure, at various times.

of the jet. In Fig. 30(a), a vortex can be seen below the jet at the jet–body interface. At this point, the jet is moving downwards, affected by the lower pressure of the vortex. A vortex above the jet forms in Fig. 30(b), which is the point where the jet is nearly normal to the body surface and the surface pressure and heating rates are at a maximum. The upper vortex grows in Fig. 30(c) as the lower vortex is shed and the jet moves upwards, pulled by the lower pressure of the upper vortex, which is itself shed into the flow in Fig. 30(d) where it gets convected along the shear layer and gradually dissipates. As the upper vortex progresses along the upper shear layer in Figs. 30(c) and 30(d), its lower pressure creates an expansion region in the layer, as can be seen by the growth of the layer and the spreading of the streamlines in the shear layer ahead of the upper vortex in Figs. 30(c) and 30(d). In order to turn the flow back in line with the body surface, a shock is formed within the shear layer and progresses through the layer just ahead of the vortex. This shock forms near the body at about the $y=0$ point, and creates a high pressure region ahead of the vortex. This can be seen in the pressure contours in Fig. 30(c). In Figs. 30(c) and 30(d), the shock travels with the flow ahead of the vortex. During this span, the lower vortex weakens and eventually dissipates as shown in the streamlines of Fig. 30(d).

This vortex shedding is consistent with prior findings for ideal gases.[7] However, unlike the ideal gas case, the present case shows vortices being shed from both the upper and lower surfaces of the jet. The two vortices are shed out of phase with each other, as can be seen in Figs. 30(b) to 30(d). This out of phase vortex shedding, shown schematically in Fig. 31, was the mechanism behind the flow unsteadiness.

D. Real-gas effects

The nonequilibrium nature of the flow fields is shown in the instantaneous dissociated nitrogen mass fraction contours in Fig. 29. As shown in these contours, there is significant variation in N composition throughout the flow field at various times. The maximum N mass fraction observed was 0.12 just behind the terminating jet shock adjacent to the body in Fig. 29(b). The region showing the next highest degree of dissociation was the area behind the upper bow shock where it was almost normal to the freestream. N mass fractions in this region reached as high as 0.10. The jet, on the other hand, was essentially frozen because the transmitted oblique shock was considerably weaker than the bow shocks. In Fig. 29(b), a disturbance of high N concentration can be seen forming just behind the terminating jet shock. This disturbance travels along the upper surface in Figs. 29(b) through 29(d). Behind this, a region of low N concentration is shed in to shear layer when the jet begins to turn upwards in Fig. 29(c). These concentration disturbances are then convected off through the shear layer.

The structure of the flow field changes drastically in the presence of real-gas effects. For example, there is a dramatic decrease in shock stand off distance in the real-gas case compared to an ideal gas case, and thus large changes in jet length. The real-gas effects in the present case can be seen through comparison with the ideal gas case studied by Zhong.[4] The levels of both heat transfer and peak surface pressure enhancement were lower for the real-gas computations. As mentioned earlier, the peak surface heating rate enhancement ratio (the ratio of peak heating to the peak heating rate without the impinging oblique shock) for the real-gas computations was 17.5. The corresponding peak pressure enhancement was 9.65. On the other hand, the ideal gas case resulted in ratios of 20 and 12.1, respectively. This reduction in the heat transfer and pressure load enhancement due to real-gas effects is qualitatively similar to Sanderson's analysis of stagnation point heat transfer rates using the Fay–Riddell model[15] for a nonequilibrium flow. Therefore, the real-gas effects reduce the peak surface heating rate and surface pressure of the type IV interference heating flows.

VII. SUMMARY AND CONCLUSIONS

The real-gas effects on two-dimensional steady shock-wave/boundary layer and unsteady type IV shock interference interactions have been studied using numerical simulations. For the steady shock/boundary layer interaction on a

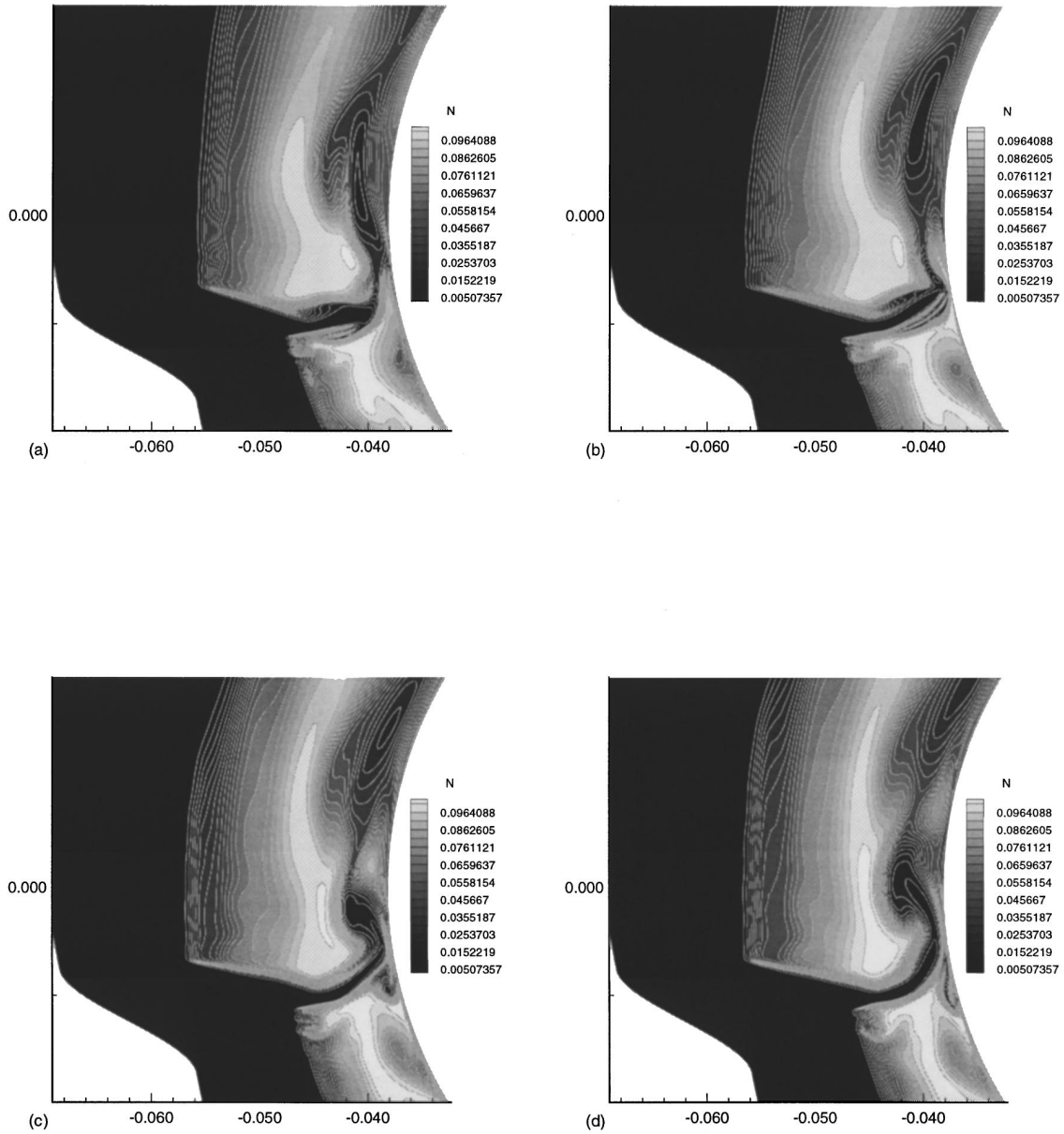

FIG. 29. Instantaneous contours of N mass fractions corresponding to various points in Figure 26: (a) frame 5, (b) frame 21, (c) frame 35, (d) frame 45.

flat plate, the real-gas effects were studied by comparing results of three different models, ideal gas, vibrationally excited but chemically frozen, and full thermo-chemical nonequilibrium models. Meanwhile, four cases with different freestream enthalpy were computed to study the effects of thermo-chemical nonequilibrium at different enthalpy levels. For the unsteady type IV shock–shock interference heating flow, an unsteady case was studied to study the real-gas effects on the unsteady mechanism of the shock–shock interference flow.

In the steady shock/boundary layer interaction, the effect of thermo-chemical nonequilibrium was found to reduce the surface heating rates and the size of the shock induced separation region. For the real gas model, raising the freestream temperature also showed the same trends. For sufficiently high freestream enthalpy, temperatures at the shock impingement point near the back of the separation bubble were high enough to cause significant nitrogen dissociation in addition to the oxygen dissociation present in the cooler flows. This additional dissociation sustained the adverse pressure gradient behind the impinging shock further than in the lower enthalpy flows, thus causing the separation region to grow in size relative to the cooler flow cases.

For the type IV shock interference heating problem, the unsteadiness was found to be related to the development and shedding of vortex structures near the jet–wall interface. The unsteadiness was the result of alternating shed vortices both above and below the jet. The effect of thermo-chemical nonequilibrium reduces peak heating and peak pressure enhancement relative to ideal gas results, which are consistent with available analytical results.

VIII. FURTHER STUDIES

A parametric study on the effects of impinging shock location and degree of nonequilibrium will be carried out to

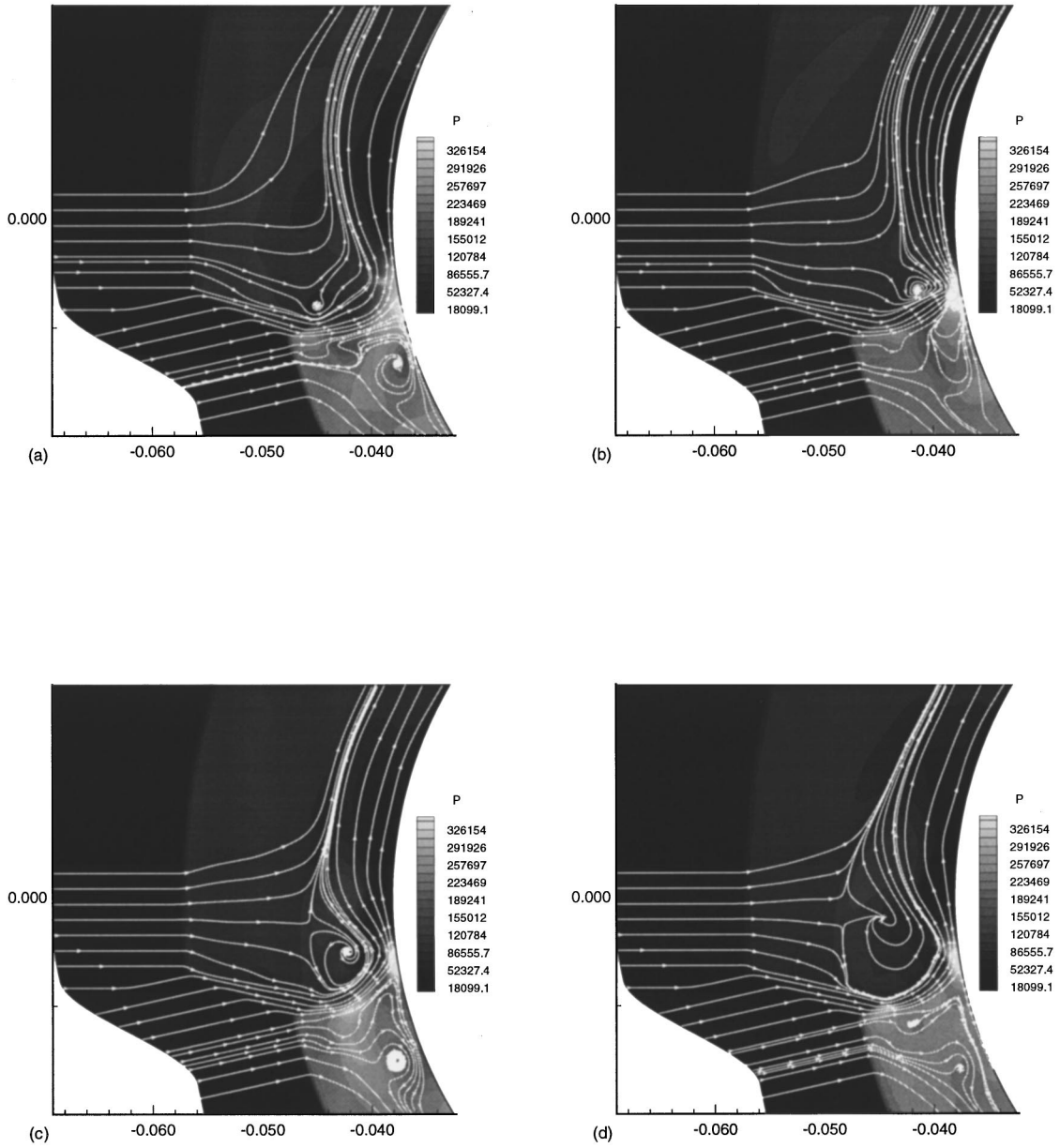

FIG. 30. Instantaneous pressure contours and streamlines corresponding to various points in Figure 26: (a) frame 5, (b) frame 21, (c) frame 35, (d) frame 45.

further understand the influence real-gas effects have on these flows. The popular Park chemistry model for air[19] will be added.The current transport models for mass diffusion and vibrational thermal conductivity are rather simplistic. They were chosen because they were the simplest accepted models available. New models for multicomponent diffusion and thermal conductivity based on the work of Gupta *et al.*[24] have been examined and will be implemented in future work.

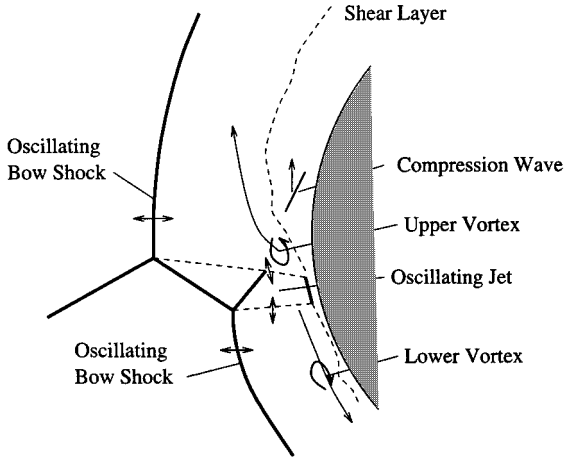

FIG. 31. Schematic of the vortex shedding mechanism responsible for the unsteadiness of the flow. The two vortices are shed out of phase with respect to each other. The arrows indicate the motions of the flow structures.

ACKNOWLEDGMENTS

This research was supported by the Air Force Office of Scientific Research under Grants No. F49620-94-1-0019 and No. F49620-95-1-0405 monitored by Dr. Len Sakell. Cray C916 and YMP-8 CPU time was provided by the CEWES High Performance Computing Center. The authors would like to thank Dr. Stefan Brück of the DLR Institute of Fluid

Mechanics for a preprint of his paper. More information on this work and related ongoing research can be found on the WWW at http://cfdlab5.seas.ucla.edu.

[1]B. Edney, ''Anomalous heat transfer and pressure distributions on blunt bodies at hypersonic speeds in the presence of an impinging shock,'' Aeronautical Research Institute of Sweden, FFA Report No. 115, 1968.
[2]A. R. Wieting and M. S. Holden, AIAA J. **27**, 1557 (1989).
[3]M. S. Holden, ''Shock–shock boundary layer interaction,'' AGARD Report No. 764, 1989.
[4]X. Zhong, AIAA J. **32**, 1606 (1994).
[5]G. H. Klopher and H. C. Yee, ''Viscous hypersonic shock-on-shock interaction on blunt cowl lips,'' AIAA Paper No. 88-0233, 1988.
[6]G. Gaitonde and J. S. Shang, ''The performance of flux-split algorithms in high-speed viscous flows,'' AIAA Paper No. 92-0186, 1992.
[7]C. A. Lind and M. J. Lewis, ''A numerical study of the unsteady processes associated with the Type IV shock interaction,'' AIAA Paper No. 93-2479, 1993.
[8]J. Delery, ''Shock/shock and shock wave/boundary layer interactions in hypersonic flows,'' in *Aerothermodynamics of Hypersonic Vehicles*, AGARD Report No. AGARD-R-761, 1989.
[9]J. J. D. Anderson, *Hypersonic and High Temperature Gas Dynamics* (McGraw-Hill, New York, 1989).
[10]J. W. Keyes and F. D. Hains ''Analytical and experimental studies of shock interference heating in hypersonic flows,'' NASA Tech. Note D-7139, 1973.
[11]G. V. Candler, ''On the computation of shock shapes in nonequilibrium hypersonic flows,'' AIAA Paper No. 89-0312, 1989.
[12]C. A. Ballaro and J. J. D. Anderson, ''Shock strength effects on separated flows in non-equilibrium chemically reacting air shock wave/boundary layer interaction,'' AIAA Paper No. 91-0250, 1991.
[13]A. A. Grumet, J. J. D. Anderson, and M. J. Lewis, ''A numerical study of shock wave/boundary layer interaction in nonequilibrium chemically reacting air: The effects of catalytic walls,'' AIAA Paper No. 91-0245, 1991.
[14]R. K. Prabhu, J. R. Stewart, and R. R. Thareja, ''Shock interference studies on a circular cylinder at Mach 16,'' AIAA Paper No. 90-0606, 1990.
[15]S. R. Sanderson, ''Shock wave interaction in hypervelocity flow,'' Ph.D, thesis, California Institute of Technology, 1995.
[16]S. Brück, ''Investigation of shock–shock interactions in hypersonic reentry flows,'' presented at the 20th International Symposium on Shock Waves, 1995.
[17]G. V. Candler, ''The computation of weakly ionized hypersonic flows in thermo-chemical nonequilibrium,'' Ph.D. thesis, Stanford University, 1988.
[18]T. Gökçen, ''The computation of hypersonic low density flows with thermochemical nonequilibrium,'' Ph.D. thesis, Stanford University, 1989.
[19]C. Park, *Nonequilibrium Hypersonic Aerothermodynamics* (Wiley–Interscience, New York, 1990).
[20]X. Zhong, ''New high-order semi-implicit Runge–Kutta schemes for computing transient nonequilibrium hypersonic flow,'' AIAA Paper No. 95-2007, 1995.
[21]W. G. Vincenti and C. H. Kruger, *Introduction to Physical Gas Dynamics* (Wiley, New York, 1965).
[22]J. N. Moss, G. A. Bird, and V. K. Dorga, ''Nonequilibrium thermal radiation for an aerospace flight experiment vehicle,'' AIAA Paper No. 88-0081, 1988.
[23]C. R. Wilke, J. Chem. Phys. **18**, 517 (1950).
[24]R. Gupta, J. M. Yos, R. A. Thompson, and K. P. Lee, ''A review of reaction rates and thermodynamic transport properties for an 11-species air model for chemical and thermal nonequilibrium calculations to 30000K,'' NASA Report No. RP-1232, 1990.
[25]J. Häuser, J. Muylaret, H. Wong, and W. Berry, ''Computational aerothermodynamics for 2d and 3d space vehicles,'' in *Computational Methods in Hypersonic Aerodynamics*, edited by T. K. S. Murthy (Kluwer–Academic, Dordrecht, 1991).
[26]R. C. Millikan and D. R. White, J. Chem. Phys. **12**, 3209 (1963).
[27]C. Park, J. Thermophys. Heat Transfer **3**, 233 (1989).
[28]L. C. Hartung, R. A. Mitcheltree, and P. A. Gnoffo, J. Thermophys. Heat Transfer **8**, 244 (1994).
[29]P. L. Roe, Annu. Rev. Fluid Mech. **18**, 337 (1986).
[30]B. Grossman and P. Cinella, ''Flux split algorithms for hypersonic flows,'' in Ref. 25.
[31]D. Gaitonde and J. S. Shang, AIAA J. **31**, 1215 (1993).
[32]B. Grossman and P. Cinella, J. Comput. Phys. **88**, 131 (1990).
[33]R. J. Leveque, *Numerical Methods for Conservation Laws* (Birkhäuser, Basel, 1992).
[34]G. H. Furumoto, X. Zhong, and J. C. Skiba, ''Unsteady shock-wave reflection and interaction in viscous flows with thermal and chemical nonequilibrium,'' AIAA Paper No. 96-0107, 1996.
[35]H. G. Hornung, J. Fluid Mech. **53**, 149 (1972).
[36]S. Shahpar, A. Kennaugh, I. M. Hall, and D. I. A. Poll, ''Comparison of computation and experiment for a high enthalpy, heated-driver, shock-tube environment,'' in *Theoretical and Experimental Methods in Hypersonic Flows*, AGARD Report No. AGARD-CP-514, 1993.
[37]J. Olejniczak, G. V. Candler, M. J. Wright, H. G. Hornung, and I. A. Leyva, ''High enthalpy double-wedge experiments,'' AIAA Paper No. 96-2238, 1996.
[38]C. Chiu and X. Zhong, ''Simulation of transient hypersonic flow using the ENO schemes,'' AIAA Paper No. 95-0469, 1995.